Granular Matter (2025) 27:19
https://doi.org/10.1007/s10035-024-01488-2

RESEARCH

3D waveforms and patterning behavior in thin monodisperse and multidisperse vertically-vibrated layers

Peter Watson[1] · Sebastien Vincent Bonnieu[2] · Ali Anwar[1,3] · Marcello Lappa[1]

Received: 15 May 2024 / Accepted: 13 November 2024

Abstract
Vibrofluidization in monodisperse granular materials is a hierarchical phenomenon involving different spatial and temporal behaviors, known to produce macroscopic structures with well-defined properties and high reproducibility. However, as witnessed by the paucity of relevant results in the literature, investigating the collective organization of particles across such different length and time scales becomes particularly challenging when multi-component systems are considered, i.e. if the considered vibrated material is not monodisperse. In this work, this problem is addressed through numerical simulation of the governing equations accounting for (dissipative) inelastic and frictional effects in the framework of a DEM (Discrete Element Method) method. Binary and ternary particle distributions are considered and, in order to filter out possible density-driven particle segregation or mixing mechanisms, particles are assumed to be iso-dense. The problem is initially analyzed through the coarse-grained lens of patterning behavior (supported by a Voronoi analysis for many representative cases) and then from a micromechanical level in which statistical data based on particle collisions and related dissipative effects are used to gain additional insights into the observed macroscopic trends. It is found that, starting from the initial traditional monodisperse case, the addition of particles with smaller sizes (while keeping the overall mass and depth of the considered layer almost unchanged) generally leads to a corrugation in the otherwise perfect symmetry of the original patterns, which is similar to that already seen in companion situations related to viscoelastic fluids. Moreover, while in the case of an initially hexagonal pattern, this topology is generally retained, in other situations, the initial perfection is taken over by less regular waveforms. Specific circumstances also exist where the initial square symmetry is lost in favor of a triangular symmetry. In all cases, segregation effects simply manifest as a preferential concentration of particles with larger size in an intermediate layer, which apparently behaves as a cohesive entity during each vibration cycle.

Keywords Granular materials · Vibrations · Fluidization · Flowability · Symmetry breaking

1 Introduction

Self-organization in granular materials is a fascinating and complex area of research within the more general field concerned with pattern formation in non-linear systems. It explores how ordered structures can emerge spontaneously when such materials are subjected to other external forces in addition to gravity. The response that they exhibit to external stimuli of various kinds is not only intriguing from a scientific perspective but also finds practical applications in various fields, including geophysics, materials science and other industrial processes.

In such a context, in particular the "ensemble" dynamics of solid particle systems are of great interest when the aforementioned mechanical stimuli are applied in the form of "vibrations" with well-defined frequency and amplitude

✉ Marcello Lappa
marcello.lappa@strath.ac.uk

[1] Department of Mechanical and Aerospace Engineering, University of Strathclyde, James Weir Building, 75 Montrose Street, Glasgow G1 1XJ, UK

[2] European Space Agency, European Space Research and Technology Centre, Keplerlaan 1, 2201 AZ Noordwijk, The Netherlands

[3] Weir Advanced Research Centre, 9 George Street, Glasgow G1 1RD, UK

Published online: 24 December 2024

[1–3]. This interest essentially stems from the possibility to translate the fundamental information gained from these studies into useful knowledge. As an example, investigating the behavior of granular materials under vibration is crucial for understanding the mechanics of earthquakes and landslides [4]. Granular materials can replicate the behavior of fault lines and help researchers gain insights into seismic activities [5]. Moreover, pattern formation in vibrated granular materials can shed light on other natural phenomena, such as the formation of sand dunes [6], ripples in rivers, soil erosion [7] and even space geology [8]. Related principles are also applied in the manufacturing industry to optimize processes like particle sorting and the formation and compaction of granular layers in products, especially in the pharmaceutical field [9, 10] and in powder metallurgy applications [11, 12]. Furthermore, the study of these aspects helps in designing processes involving particulate or granular flows in mineral processing [13,–15], in mining industries [16] and many other circumstances related to powder mixing and transport [17–19]. Other interesting links can also be found with regard to agriculture, where a proper knowledge of granular material behavior is instrumental in optimizing seed distribution systems and efficient planting [20] or it can support related food processing activities [21, 22].

As outlined at the beginning of this section, however, it is clear that, beyond practical applications, these subjects also exert an appeal to researchers and scientists because they are often regarded (or used) as paradigms to understand the relationship between "order" and "chaos" and/or between macroscopic and microscopic dynamics. These specific aspects often make this category of problems irresistible to theoretical physicists and mathematicians. The crucial point is about understanding what provides these systems with their specific macroscopic properties, that is, what they can do as a result of the mutual interplay of the constitutive parts, which such parts would not able to do if considered separately. A related concept is that about the relationship between the considered system and its "environment", which brings in the role of "boundary conditions" as an additional factor influencing the possible behaviors, i.e. the system "function".

In other words, studies of such a kind have often been conducted essentially in the attempt to distillate common trends out of seemingly disparate dynamics, that is, trying to discern the general laws or principles out of which similar patterning behaviors can be produced in different conditions or fields.

In this regard, it is worth mentioning that the behavior of granular materials shares many aspects with the companion field of "fluid-dynamics" [23–25]. Indeed, granular materials are often regarded as a special category of "fluids" or even "gases" [26, 27], which in addition to *frictional effects* have a secondary dissipation mechanism strictly related to the *inelastic nature of the collisions* occurring among grains (and/or with the solid boundary of the related container). As the reader might have realized at this stage, both fluids and granular materials can be seen as specific examples of systems consisting of collections of sub-parts (molecules in the case of fluids, solid particles in the case of granular materials) for which related "dissipative effects" play a crucial role. It is just by virtue of such energy-degradation mechanisms that these systems are provided with the ability to develop a hierarchy of phenomena and ensuing collective behaviors. Indeed, "self-organization" is a typical outcome of processes that are governed by a global driving force injecting energy into them at a "macroscopic" level and "local" forces able to dissipate it at a smaller scale.

The affinity with the behavior of fluids goes some way to explain why this subject has been largely studied resorting to typical concepts and tools traditionally used in the context of fluid-dynamic analyses. Relevant examples of this modus operandi include the theory of bifurcations, whose typical jargon has been extensively applied to characterize phenomena in vibrated granular materials (in particular, the notions of wavelength, waveform, cellular pattern and "hierarchy of bifurcations"). "Amplitude equations" able to account for the weakly non-linear behavior of these systems not too far from bifurcation points have also been used to a certain extent (see, e.g [28]).

Although such concepts and tools have enjoyed quite a widespread use, it is worth recalling that, in general, granular materials do not obey the same equations or relationships that characterize fluids [29]. Although some valuable efforts in this direction exist, reliable and universally accepted models able to relate the macroscopic stresses at play in granular materials to the exchange of momentum occurring at a microphysical scale have not emerged yet. In general, the stress tensor for these materials consists of two distinct terms, one accounting for the contact forces existing within adjoining particles and a second contribution stemming from purely dynamic effects [25, 30, 31].

The differences existing between fluids and granular materials at a microscopic scale typically reverberate at larger scales, thereby setting some differences between these two categories of matter (at least in terms of non-linear behavior). Typically,, the dimensionality of the space of parameters is generally larger for granular material in comparison to the equivalent one in the case of fluids. Solid particles or grains constituting granular materials can exhibit a variety of shapes and sizes. Although, for simplicity, most existing studies have assumed spherical grains and monodisperse distributions (i.e. collection of spherical particles

all having the same size), these should be regarded as special cases or particular realizations.

Owing to space limitations, obviously, we do not strive to review all the interdependences and aspects of this complex problem. Along these lines, what follows should be regarded as a focused review of existing studies on vertically vibrated monodisperse granular layers where the system response and patterning behavior have been investigated for increasing values of the "forcing" (i.e. the amplitude of the vibrationally induced acceleration) and the related frequency.

After the seminal work by Thomas et al. [32] and many other important papers, where a first categorization of the observed dynamics was introduced, relevant and valuable examples of this line of inquiry are the works by Melo et al. [33, 34], Umbanhowar et al. [35], Tsimring and Aranson [28] and Bizon et al. [36]. We apologize to all whose work is not included in this synthetic account. This list is not intended to be exhaustive, but rather to stimulate the interest of the reader in certain aspects, some longstanding, some new, where advances are needed. In particular, the greatest merit of these studies resides in having removed the constraint of narrow containers (i.e. having one horizontal dimension much smaller than the other). This simplification had been largely used in earlier investigations where the focus was on two-dimensional patterning behaviors rather than three-dimensional (3D) effects.

Taken together, all these analyses have revealed a variety of interesting 3D patterns obeying different symmetries and/or morphologies, enabled by different combinations of the considered influential patterns. The main motivation at the root of the present work is an extension of these earlier important findings to the fundamental situation, in which, although all the particles retain a spherical shape and are made of the same material, however, they are present with different radii at the same time. In order to support reader's understanding of such dynamics, systems of growing complexity are treated as the discussion progresses, i.e., starting from well-established results in the monodisperse case, then situations are considered in which a bi-disperse (binary) or three-disperse (ternary) distribution of particles is involved. As we focus on either a fixed number of layers or a fixed amount of material, the problem is investigated in the framework of numerical simulations.

2 Mathematical Model

In particular, in the present study, the problem related to the evolution in time of the considered distribution of particles and ensuing patterning behavior under the effect of vibrations is addressed in the framework of a DEM (Discrete Element Method) strategy. Since, as outlined in the introduction, there are specific properties of granular media that prevent them from being properly described as a fluid or more generally as a "continuum", this specific approach conveniently relies on a formulation where every particle present in the system is tracked *separately*, that is, a *Lagrangian perspective* is used. Put simply, when the particles move in the considered physical domain under the effect of the applied forces (gravity and acceleration induced by vibrations in the present case), particles undergo translational and rotational dynamics, which are properly modeled in the framework of classical Newtonian physics.

2.1 Governing equations

From a practical standpoint, two distinct vector equations are used to deal with the six degrees of freedom (3 translational and 3 rotational) of each particle (see, e.g., Guo and Curtis [37]; Kieckhefenet al. [38] and El Emam et al. [39]). In vector notation and in a laboratory reference system these equations simply read:

$$m_i \frac{d^2 \underline{r_i}}{d\tau^2} = \underline{F_i^g} + \sum_{j=1}^{N} \underline{F_{ij}^c} \tag{1}$$

$$I_i \frac{d\underline{\omega_i}}{d\tau} = \sum_{j=1}^{N} \underline{M_{ij}^c} \tag{2}$$

where τ is the physical time, m_i is the generic particle mass, the vectors $\underline{r_i}$ and $\underline{\omega_i}$ account for its position and angular velocity, respectively, $\underline{F_i^g}$ is the body force acting on each particle due to the effects of gravity, $\underline{F_{ij}^c}$ is the contact force exerted by the generic particle j on the considered i particle, I_i is the moment of inertia of the particle i and, by analogy with $\underline{F_{ij}^c}$, $\underline{M_{ij}^c}$ is the moment that the particle j exerts on particle i (in this study no interstitial fluid is simulated, which explains why, no forces of fluid-dynamic nature are considered).
The gravitational force can be expressed in a relatively simple way as:

$$\underline{F_i^g} = m_i \underline{g} \tag{3}$$

where g is the gravity acceleration (9.81 ms^{-2} on the surface of Earth). The presence of vibrations can be taken into account by setting a time-periodic displacement for the physical boundary of the particle container, i.e.:

$$\underline{s}^{vibr} = b \sin(\Omega\tau)\underline{\widehat{\kappa}} \tag{4}$$

where b and Ω are the amplitude and the angular frequency of the imposed vibrations, respectively and $\underline{\widehat{\kappa}}$ is the unit vector along the direction of vibrations. In a particle-container based reference system, an acceleration is produced accordingly, which can be cast in condensed form as:

$$\underline{a}_{\omega}(\tau) = \underline{\ddot{s}}(\tau) = -a_{\Omega}\sin(\Omega\tau)\underline{\widehat{\kappa}} \tag{5}$$

where obviously $a_{\Omega}=b\Omega^2$ (resulting from two consecutive derivations in time of the original displacement function). This indicates that in a container based reference system, the effect of vibrations can be seen as a time-varying acceleration with amplitude given by the product of b and the square of the angular frequency $\Omega = 2\pi f$. The overall acceleration acting on the particles can therefore be expressed as:

$$\underline{a}(\tau) = \underline{g} - a_{\Omega}\sin(\Omega\tau)\underline{\widehat{\kappa}} \tag{6}$$

Equation (6) is instrumental in showing that vibrations do not contribute to any time-averaged acceleration or force, as mathematically demonstrated by the following identity [40]:

$$\begin{aligned}\underline{a}_{average} &= \frac{\Omega}{2\pi}\int_0^{2\pi/\Omega}\underline{a}(\tau)d\tau = \frac{\Omega}{2\pi}\int_0^{2\pi/\Omega}\underline{g}d\tau + \frac{\Omega}{2\pi}\int_0^{2\pi/\Omega}a_{\Omega}\sin(\Omega\tau)\underline{\widehat{\kappa}}d\tau \\ &= \frac{\Omega}{2\pi}\underline{g}\int_0^{2\pi/\Omega}d\tau + \frac{\Omega}{2\pi}a_{\Omega}\underline{\widehat{\kappa}}\int_0^{2\pi/\Omega}\sin(\Omega\tau)d\tau = \underline{g} - \frac{1}{2\pi}a_{\Omega}\underline{\widehat{\kappa}}[\cos(\Omega\tau)]_0^{2\pi/\Omega} = \underline{g}\end{aligned} \tag{7}$$

2.2 Inelastic and frictional effects

The particle-to-particle and particle-to-boundary effects are accounted for by resorting to specific interaction models, as further illustrated in the following. The DEM generally calculates this force for spherical particles as the combination of two distinct contributions, one of elastic-plastic nature ($\underline{F}_{ij}^{n}$) and another one ($\underline{F}_{ij}^{t}$) essentially related to frictional effects:

$$\underline{F}_{ij}^{c} = \underline{F}_{ij}^{n} + \underline{F}_{ij}^{t} \tag{8}$$

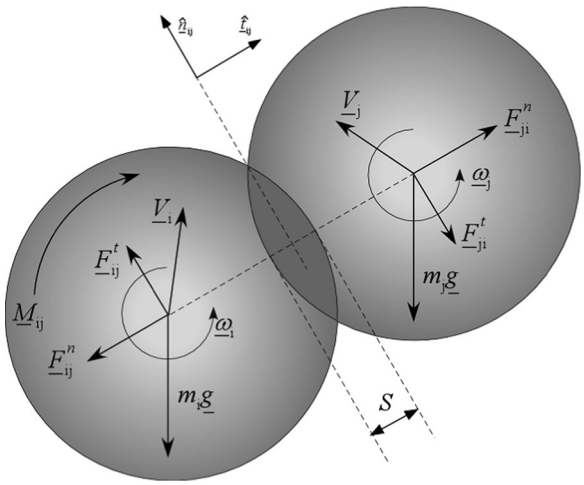

Fig. 1 Sketch of interacting particles and related kinematic and dynamic quantities

A proper derivation of these forces requires recalling the distinction between the so-called hard-sphere and soft-sphere models. With the former, particles are treated as rigid spheres, which means no deformation and/or overlap is allowed. As a natural consequence, contact forces along the direction passing through the centers of two interacting particles (hereafter simply referred to as normal direction and identified using the "n" superscript) are generally implemented as "impulsive" forces (see, e.g., Stratton et al. [41]; Richardson et al. [42]). By contrast, with the soft-sphere model, although particles are still assumed to be undeformable, a certain overlap is allowed (Fig. 1). This artifice leads to a straightforward derivation of the force $\underline{F}_{ij}^{n}$ induced in the normal direction by the particle-to-particle interaction. Indeed, a precise relationship is generally introduced between the intensity of such a force and the overlap extent (see, e.g., Schwartz et al. [43]; Murphy et al. [44]; El Emam et al. [39]). Put simply, DEM relies on virtual rigid springs, acting perpendicularly to the contact plane to calculate such a force. This approach, in turn, stems from the so-called Hertzian Model originally introduced by Hertz in the nineteenth century by which the normal force is evaluated by considering the response of two elastic spheres in contact over a small circular area, and a proper damping contribution is also introduced to account for dissipative effects. The model can therefore predict a normal force that is essentially repulsive, and it also allows energy dissipation. A notable extension of this strategy is due to Walton and Braun [45]. These authors adopted a different philosophy to properly take into account *hysteretic effects*, i.e. the asymmetry in the force evolution during the loading and unloading stages of the particle-to-particle interaction process, which is typically due to plastic (i.e. irreversible) phenomena. In place of using a complex elastic-damping spring model, with this alternate approach, the shape of overlap-normal force is approximated by a linear law, however, different slopes are considered for the loading and the unloading stages, as shown in Fig. 2.

As evident in this figure, while the linear loading branch has a slope K_l^n, the slope K_u^n of the unloading branch is steeper. This obviously results in a "residual displacement" (S_o) when in the unloading stage the normal force is reduced to zero (Walton [46]; see again Fig. 2), which can be regarded as a consequence of plastic effects. Notably, the area between the two branches represents the energy lost accordingly. In other words, as explained before, although there is

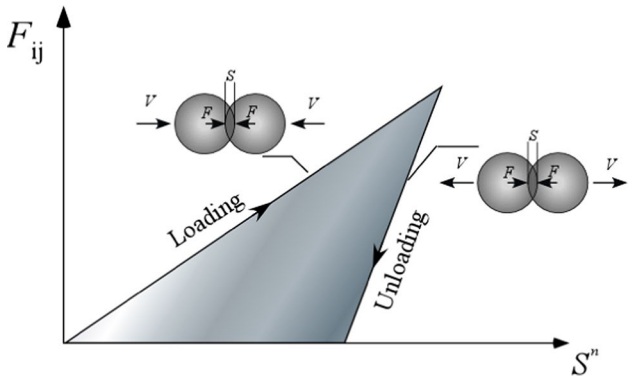

Fig. 2 Sketch of particle loading-unloading asymmetry used to account for inelastic effects

no change of particle shape or size, the model assumes that some particle overlap is possible. Put simply, from a purely numerical point of view, the distance between the centers of two interacting spherical particles is allowed to become smaller than the summation of the two interacting particles radii. In this stage, particle kinetic energy can be dissipated (i.e. the algorithm based on the equations reported in the following allows degradation of particle kinetic energy, that is, a fraction of this energy is consumed in this process, the reader being referred to Sect. 2.3 for an expression for this fraction). From a purely mathematical point of view, the energy lost in this way depends on the particle physical properties and the related "restitution coefficient" (see Eqs. (9–12)). These are typically determined experimentally and used in the numerical simulations. From an algorithm standpoint, the Rocky software (used for this study) implements this model as follows [47–49]

$$\underline{F}_{ij}^{n,(\tau)} = \begin{cases} \min\left(\underline{F}_{ij}^{n,(\tau-\Delta\tau)} + K_u^n \underline{\Delta S}^n, K_l^n \underline{S}^{n,(\tau)}\right) if \Delta S^n \geqslant 0 \\ \max\left(\underline{F}_{ij}^{n,(\tau-\Delta\tau)} + K_u^n \underline{\Delta S}^n, K_l^n \underline{S}^{n,(\tau)} x 10^{-3}\right) if \Delta S^n < 0 \end{cases} \tag{9a}$$

$$\underline{\Delta S}^n = \underline{S}^{n,(\tau)} - \underline{S}^{n,(\tau-\Delta\tau)} \tag{9b}$$

where $\underline{F}_{ij}^{n,(\tau)}$ and $\underline{F}_{ij}^{n,(\tau-\Delta\tau)}$ represent the normal contact force at the time (τ) and (τ-$\Delta\tau$), respectively and $\underline{\Delta S}^n$ is the corresponding variation undergone by the overlapping during the timeframe $\Delta\tau$. The scale factor 10^{-3} appearing in Eq. (9a) is used to ensure that that the force becomes negligible in the limit as the overlap tends to zero.

The loading and unloading stiffness appearing in Eq. (9a) can be evaluated as:

$$\frac{1}{K_l^n} = \frac{1}{K_{li}^n} + \frac{1}{K_{lj}^n} \rightarrow K_l^n = \frac{K_{li}^n K_{lj}^n}{K_{li}^n + K_{lj}^n} \tag{10a}$$

$$\frac{1}{K_l^n} = \frac{1}{K_{li}^n} + \frac{1}{K_{lwall}^n} \rightarrow K_l^n = \frac{K_{li}^n K_{lwall}^n}{K_{li}^n + K_{lwall}^n} \tag{10b}$$

for the particle-to-particle (Eq. (10a)) and particle-to-wall interaction (Eq. (10b)), respectively, where

$$K_{li}^n = E_i d_i \tag{11a}$$

$$K_{lwall}^n = E_{wall} d_i \tag{11b}$$

and E_i and E_{wall} are the Young's modulus of the particle and wall materials, respectively and d_i is the particle size. With such an approach, the coefficient of restitution ε, related from a physical standpoint to the dissipated energy shown in Fig. 2, can be expressed as:

$$\varepsilon^2 = \frac{K_l^n}{K_u^n} \tag{12}$$

As outlined before, the DEM approach can also take into account forces which are directed in a tangential direction (hereafter, simply identified using the "t" superscript) and are essentially induced by frictional effects. In this case, the software relies on the so-called linear elastic-frictional model [47–49]. With this paradigm, the evaluation of the force differs depending on whether sliding takes place during the contact or not. Accordingly, the force can be cast in compact form as follows:

$$\underline{F}_{ij}^{t,(\tau)} = \min\left(\underline{F}_{ij}^{t,(\tau-\Delta\tau)} + K_l^n \underline{\Delta S}^t, \mu \underline{F}_{ij}^{n,(\tau)}\right) \tag{13}$$

where $\underline{F}_{ij}^{t,(\tau)}$ and $\underline{F}_{ij}^{t,(\tau-\Delta\tau)}$ represent the tangential contact force at the time (τ) and (τ-$\Delta\tau$), respectively, $\underline{\Delta S}^t$ is the corresponding change in the tangential overlapping during the timeframe $\Delta\tau$, and μ is the friction coefficient, which takes different values according to whether there is sliding between the particles or not, i.e.:

$$\mu = \begin{cases} \mu_s, if no sliding (static-coeffcient) \\ \mu_d, if sliding (dynamic-coeffcient) \end{cases} \tag{14}$$

Put simply, when the tangential force becomes larger than $\mu_s \underline{F}_{ij}^{n,(\tau)}$, sliding is enabled. As soon as the force becomes smaller than this threshold, the contact is assumed to come back to the non-sliding condition.

In the DEM software [49] all the equations above are integrated numerically using an explicit scheme in time. As each individual particle is tracked separately, the complete history of all particles inside the domain can be reconstructed (this includes, for example, velocities, and contact data), thereby allowing the user to extract information that is hardly accessible when the same problem is addressed by experimental analysis.

2.3 Integral based statistics

Most notably, the availability of the above-mentioned "historical" data allows the straightforward determination of some characteristic quantities, which generally prove very useful when one has to cope with the possible interpretation of highly non-linear dynamics. These derived quantities are essentially energy terms, whose usefulness mainly resides in the quantitative information they provide about the dissipative mechanisms at work in the considered system.

Put simply, these are: the *dissipated energy* and the *shear energy*, i.e. the mechanical energy transformed irreversibly into *internal energy* during a particle-to-particle collision essentially due to the inelastic nature of the collision itself and the work done by the tangential contact forces, respectively. The former can be expressed from a purely mathematical point of view as:

$$W_{ij}^{diss} = \int \underline{F}_{ij}^{c} \cdot \underline{V}_{ij}^{rel} d\tau \tag{15}$$

where $\underline{V}_{ij}^{rel}$ is the instantaneous relative velocity at the contact point between the particles i and j. If a rolling model is also used in the simulation, this brings in an additional contribution of dissipative nature that can be evaluated as

$$W_{ij}^{diss(roll)} = \int \underline{M}_{rel}^{c} \cdot \underline{\omega}^{rel} d\tau \tag{16}$$

where $\underline{M}_{rel}^{c}$ is the rolling resistance moment and $\underline{\omega}^{rel}$ is the relative angular velocity.
The shear energy simply reads:

$$W_{ij}^{shear} = \int |\underline{F}_{ij}^{t}| dS^{t} \tag{17}$$

In the framework of the DEM software [49], these integrals are computed using the classical trapezoidal rule. These serve as a basis for the ensuing evaluation of the dissipative and shear powers, namely:

$$P_{p}^{diss} = \frac{\sum_{k=1}^{N_k} W_{k}^{diss}}{\Delta\tau} \tag{18}$$

$$P_{p}^{shear} = \frac{\sum_{k=1}^{N_k} W_{k}^{shear}}{\Delta\tau} \tag{19}$$

where N_k represents the collisions occurring over the entire surface of a particle p during a given time interval $\Delta\tau$. Finally meaningful particle statistics can be obtained by taking the related "average", defined as:

$$P_{avg}^{diss} = \frac{\sum_{p=1}^{N_p} P_{p}^{diss}}{N_p} \tag{20}$$

$$P_{avg}^{shear} = \frac{\sum_{k=1}^{N_p} P_{p}^{shear}}{N_p} \tag{21}$$

where N_p is the total number of particles.

2.4 Non-dimensional governing parameters

The constant gravity acceleration g introduced in Sect. 2.1 is generally used as a reference quantity to define relevant non-dimensional characteristic groups or "numbers". As an example, the nondimensional vibration acceleration acting on grains (also known as "reduced dimensionless acceleration") is generally defined as:

$$\Gamma = \frac{b\Omega^2}{g} \tag{22}$$

A consistently introduced non-dimensional vibration frequency simply reads

$$f^{*} = f\sqrt{h/g} \tag{23}$$

where h is the initial depth of the granular material, initially assumed to be accumulated at the bottom of the container and have a flat top surface [36]. This depth can be used to introduce another characteristic parameter, namely:

$$\mathrm{N}_i = \frac{h}{d_i} \tag{24}$$

which for a monodisperse material can be seen as the initial "number of particle layers". In turn, the particle diameter d_i can be used to define another non-dimensional ratio in conjunction with the amplitude of vibrations b [40], namely:

$$\zeta = \frac{d_i}{b} \tag{25}$$

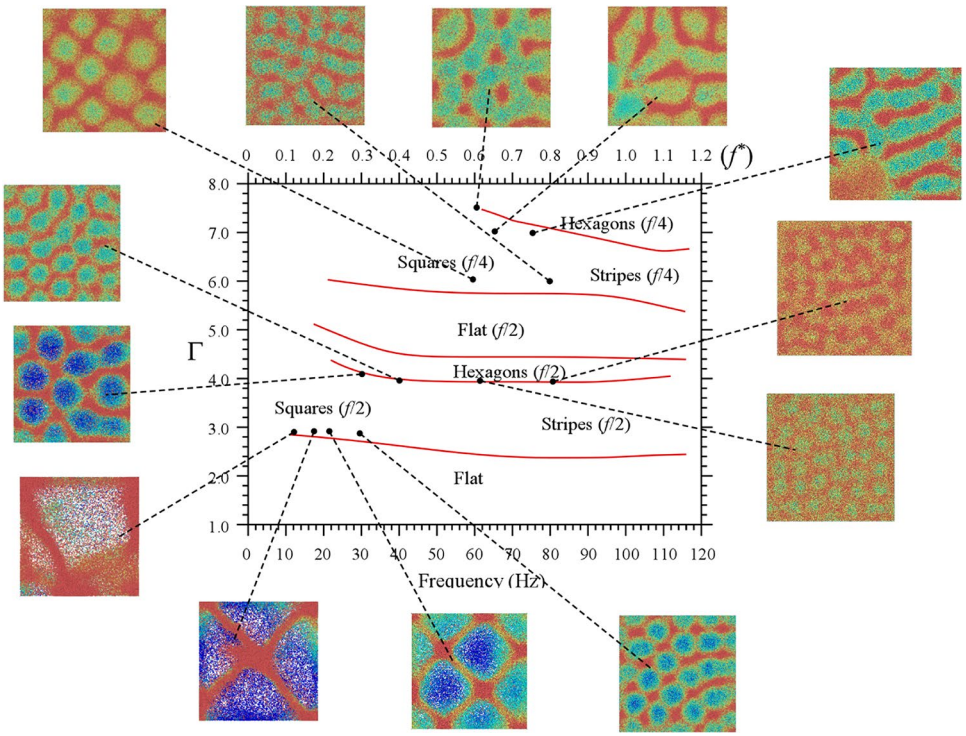

Fig. 3 Location of the present numerical results in the space of parameters with respect to the regions of existence of the different patterns originally identified in the experimental work by Melo et al. [34]

Table 1 Particle properties used for the numerical simulations

Particle properties	Corresponding values
Particle Density (kg/m^3)	8770
Youngs modulus (MPa)	100
Particle diameter d (m)	$d_1 = 1.6\times10^{-4}$ (mono-disp), $d_2 = 8\times10^{-5}$ (binary), $d_3 = 1.2\times10^{-4}$ (ternary)
Particle material	Bronze
Poisson's ratio	0.3

Table 2 Particle-particle coefficients used for the numerical simulations

Particle-Particle coefficients	Corresponding values
Static friction (-)	0.5
Dynamic friction (-)	0.45
Tangential stiffness ratio (-)	1
Coefficient of restitution (-)	0.9

Table 3 Boundary properties used for the numerical simulations

Boundary properties	Corresponding values
Boundary Density (kg/m^3)	7850
Youngs modulus (MPa)	100,000
Boundary material	Aluminium
Poisson's ratio	0.3

Table 4 Particle-boundary coefficients used for the numerical simulations

Particle-wall coefficients	Corresponding values
Static friction (-)	0.6
Dynamic friction (-)	0.55
Tangential stiffness ratio (-)	1
Coefficient of restitution (-)	0.9

3 Results

3.1 Monodisperse case

As outlined in the introduction, for the specific case of a monodisperse layer of particles vibrated vertically, earlier experimental investigations have produced a trove of data that reveal transcending characteristics across a vast space of parameters. Relevant studies along these lines include the valuable contributions by [33–36]. In these studies shallow containers were used (base area much larger that the height), thereby allowing particles to produce fascinating collective behaviors in the three-dimensional space, manifesting themselves in the form of well-defined patterns or "waveforms".

In particular, three fundamental types of morphologies were revealed, namely, patterns satisfying a square symmetry, a hexagonal symmetry or waveforms that can approximately be considered "two-dimensional" as they consist of a distribution of peaks and valleys aligned with a well-defined direction (also simply referred to as "stripes").

A relevant example of these behaviors can be gathered from Fig. 3, where we have summarized a number of numerical results obtained with the approach described in Sect. 2 for the same conditions that Melo et al. [34] originally considered for their experiments (the reader being referred to the data reported in Tables 1, 2, 3 and 4).

This figure is instructive as it provides a synthetic view of the possible patterning behaviors over a relatively extended range of the imposed shaking frequency and the vibrationally-induced acceleration. Moreover, the large number of included cases also witness the excellent agreement between the present numerical and the earlier experimental results by [34]. Notably, apart from serving as a relevant validation of the overall theoretical-numerical architecture defined in Sect. 2, this preliminary study also represents a relevant basis for the ensuing analysis (Sect. 3.2 and 3.3) where the constraint of monodisperse distribution of particles is removed. Moreover, it confirms Melo and coworkers' deduction that interstitial gas does not play a significant role in the considered dynamics (as anticipated in Sect. 2, no interstitial gas has been assumed for the present simulations).

In the numerical simulation, the dimensions of the container have been fixed to 2 cm x 2 cm along x and y, respectively (a total area of 4 cm^2), whereas a height of 12 cm has been considered (the z direction being parallel to gravity). The same particles used in the experiments have been selected (the reader being referred again to Table 1).

In order to show that the results can be considered weakly dependent on the lateral wall-effect and domain extension, numerical simulations have been repeated for some representative cases (the square and hexagonal patterns shown in Fig. 4) by doubling the domain size along the horizontal direction (a bottom area of 16 cm^2 in place of 4 cm^2). Such extra computations have shown that while the domain has no impact on the emerging pattern when moving from the 16 cm^2 to the 4 cm^2 domain, it however can cause a minor change in the wavelength in the square symmetry case, i.e. ≅10% for $\Gamma=2.9$ and $f=20$ Hz (which however we consider acceptable given the notable savings in terms of computational time obtained with the 2×2 cm^2 domain). As evident in Fig. 4b, the corresponding variations for $\Gamma=4$ and $f=40$ Hz (hexagonal pattern) are hardly detectable (being $<<1\%$).

A sequence of $N=7$ perfectly aligned and superimposed layers of particles has been assumed as the initial condition in all monodisperse cases. This specific choice in terms of initial conditions follows a precise rationale, which requires a brief excursus on the known properties of these systems.

More specifically, Melo et al. [33] reported that, in analogy with the properties of the Faraday waves in fluids, on increasing the depth of the monodisperse material, the mean wavelength λ of the pattern (close to the onset) first grows, but then it tends to a constant value (a condition that they called "*saturated state*"). Moreover, they found this value to be weakly dependent on the effective particle size (d) but to always correspond to a specific number of particle layers, i.e. $N=7$.

This specific situation may therefore be regarded as a special condition for which the number of parameters affecting the system can be somehow minimized. Indeed, for $N\geq7$, the pattern wavelength is weakly dependent on the particle size (see Fig. 3a in [33]), and can therefore be seen as a function of the frequency and the parameter Γ only.

That is why this specific configuration is considered in the present study as a relevant condition aiming at the identification of universality classes in the considered dynamics ($N=7$, $h=7d_1=1.12\times10^{-5}$ m). Some of these can be directly gathered from Fig. 3 (a diagram with the frequency f as abscissa and Γ as ordinate). Several distinct sub-domains can be clearly discerned in this figure. The first one (lower part of the plot) is the region where no specific pattern is formed. However, as soon as Γ exceeds a given threshold (≅2.2), which slightly depends on the considered frequency, particle self-organization is enabled. In particular, two different topologies are possible according to the frequency. While for relatively small frequencies and a fixed Γ (e.g., $\Gamma=2.9$), a pattern with the square symmetry is dominant, at larger frequencies, this morphology is taken over by a different waveform, consisting of an ordered series of aligned valleys and mountains, giving the observer the illusion of a series of "stripes". As shown by the various insets included

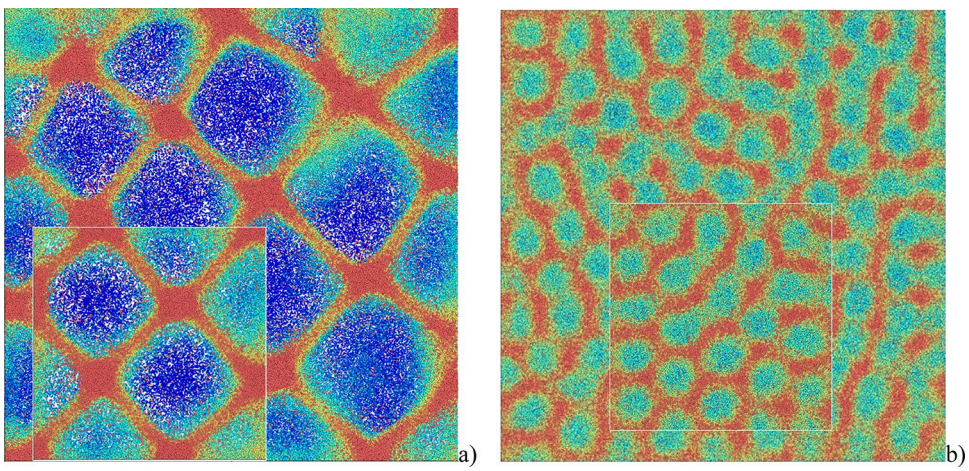

Fig. 4 Numerical simulations (monodisperse case with $N=7$) for (a) $\Gamma=2.9$ and $f=20$ Hz and (b) $\Gamma=4$ and $f=40$ Hz. Domain size 4×4 cm^2, the inset shows the corresponding results obtained for a 2×2 cm^2 domain

in this figure, intermediate cases are also possible, where the material surface displays at the same time properties that are typical of both patterns.

The emergence of all these states can be ascribed to a "period-doubling bifurcation" [33]. More specifically, while the square topology essentially stems from the superposition of two standing waves that have perpendicular wave vectors, the same amplitude and oscillate at half the driving frequency, the stripes reflect a single parametric standing wave [33]. In light of this interpretation, the intermediate states, obtained on moving (at a constant Γ) from the region where squares are dominant to that where stripes are the typical outcome, may be regarded as hybrid solutions where the aforementioned perpendicular wave vectors have different amplitudes (one wave becoming progressively dominant with respect to the other as the frequency grows).

At this stage, a further characterization of the map shown in Fig. 3 can be obtained by moving in the (Γ-*f*) plane along a line of constant *f* (a vertical traverse, in place of a horizontal line).

Let us consider for instance a traverse at $f=30$ Hz. For this frequency, a hexagonal pattern arises spontaneously from the squares reported for $\Gamma=2.9$ as soon as the considered vertical line intersects the next (red solid line) transition curve contained in this figure, i.e. if Γ is increased beyond $\Gamma=3.9$. As originally reported by [34], like squares and stripes, the hexagons also recover their initial configuration after two periods (which explains why the "*f*/2" condition also applies to them). However, unlike those patterns, they do not undergo a spatial shift of one-half wavelength after a forcing period. Rather if two consecutive forcing periods are considered, an observer would see a swap in the position of nodes and antinodes, i.e. a set of isolated peaks on a triangular lattice, which is turned during the next oscillation into hexagonal cells, each one centered on a former peak location [34].

As Γ is further increased, a region is met where no defined patterning behaviors are possible. Nevertheless, squares and stripes re-enter the dynamics as soon as another threshold is exceeded ($\Gamma\cong5.9$). For Γ overcoming this value, a new period-doubling bifurcation is enabled, thereby making the characteristic frequency of oscillation of the pattern *f*/4.

The dynamics in this situation are somehow similar to those already described for the case *f*/2. Patterns with the square topology are preferred for relatively small frequencies, whereas stripes reappear as the dominant waveform for larger *f*. Most interestingly, another narrow region also exists, where the hexagonal symmetry is recovered for larger Γ and $f>60$ Hz. However, for smaller frequencies ($f<60$ Hz), only disordered states are possible. As an example of this trend, the reader may consider a vertical transverse at $f=60$ Hz. An increase of the vibration amplitude from $\Gamma=6$ to $\Gamma=7.5$ along this vertical path causes the transition from a regular pattern with the square topology to a much less regular solution, where no specific symmetry or waveform is recognizable.

Additional insights into these behaviors directly stem from an analysis of the pattern wavelength and the related "vertical amplitude" (i.e. the maximum vertical extension of the particle distribution in space). The wavelengths and other pattern-related geometrical details have been determined through a Voronoi analysis by using the "Ka-me" image analysis software [50, 51]. In qualitative agreement with earlier findings (see, e.g., Clément et al. [52]), the present simulations have confirmed that for a fixed frequency, progressively higher values of Γ (or vice versa smaller values of the parameter ζ defined by Eq. (25)) produce larger wavelengths and vertical amplitudes. As an example, considering again a vertical transverse at $f=30$ Hz, the increase in the pattern wavelength is evident when moving from the inset for $\Gamma=2.9$ to that for $\Gamma=4$. Notably, this variation is appreciable even if a change in the pattern topology occurs (e.g. from squares to hexagons).

Another key point concerns the dependence of the wavelength on the frequency. Available experimental evidence indicates that for frequencies larger than a crossover value, the wavelength saturates at a value independent of the forcing frequency (see, e.g., Clément and Labous [53]), whereas for smaller frequencies, the wavelength and pattern amplitude essentially decrease as a function of *f*. In particular, Melo et al. [33] could show that for the square pattern and $N=7$, the wavelength was inversely proportional to the frequency of vibrations for different particle diameters.

Such trends can be qualitatively recognized in Fig. 3 for several values of Γ, e.g., $\Gamma=2.9$ (squares *f*/2), $\Gamma=4$ (hexagons *f*/2) and $\Gamma=6$ (squares, *f*/4). For more precise (quantitative) information about such dependencies, the reader is referred to Fig. 5. These figures show the pattern wavelength (left panel) and the corresponding particle distribution vertical amplitude (right panel); both are measured at a specific time, i.e. the instant at which the falling set of particles "touches" the bottom of the container (as shown, e.g., by the inset contained in the right panel of Fig. 5a and c).

A quantitatively and qualitatively substantiated by these figures, an inverse relationship with respect to the frequency (i.e. a law $\cong c/f$ where c is a constant) fits relatively well the numerically obtained data over a relatively wide range of frequencies and for different values of Γ. The tendency of the curves to attain an asymptotic regime where the considered quantity (wavelength or amplitude) becomes almost insensitive to frequency variations (the aforementioned saturated state that is attained for frequencies larger than a crossover value) can also be recognized. Figure 5a shows that, however, for relatively small values of Γ ($\Gamma=2.9$) and frequency

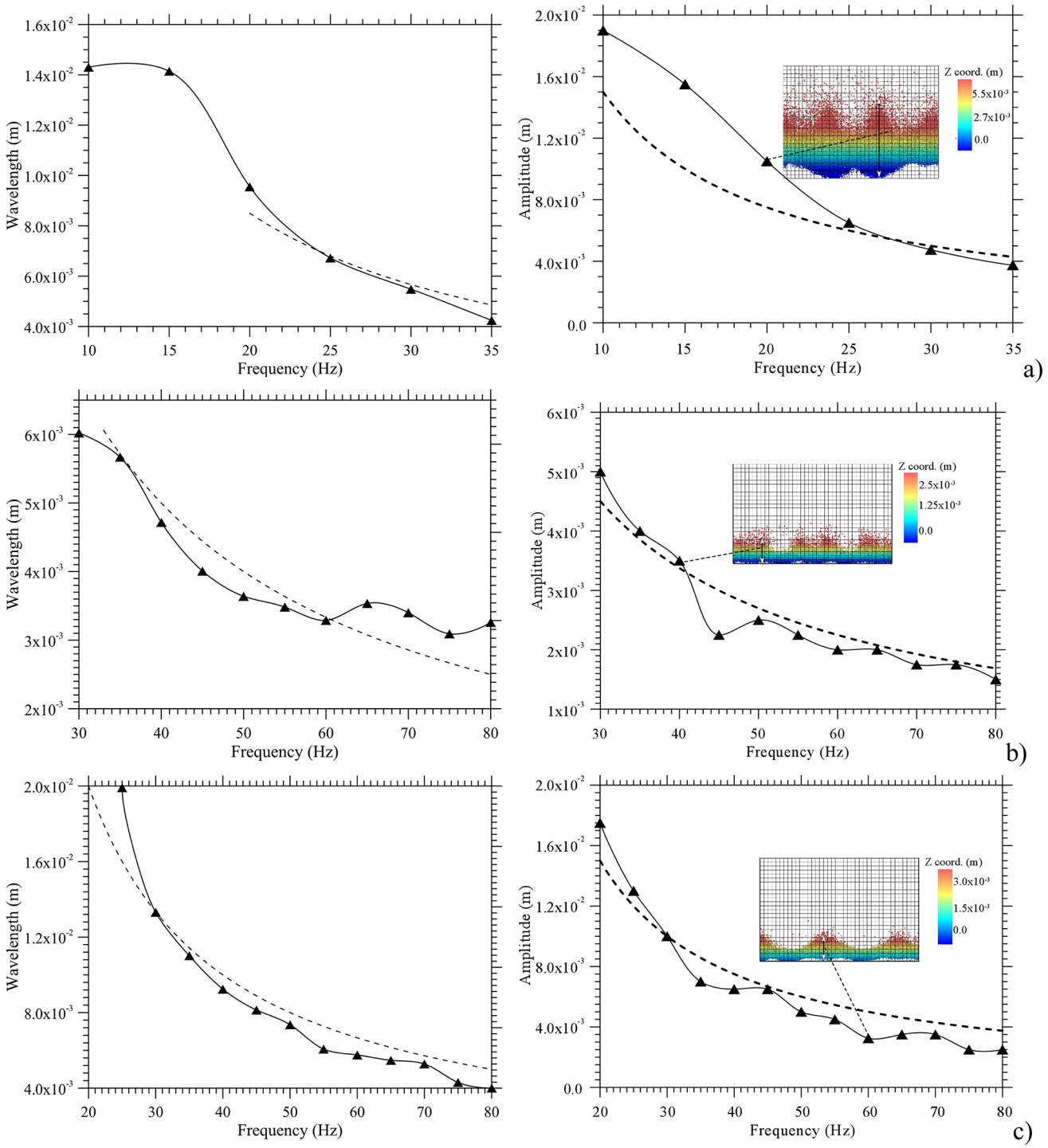

Fig. 5 Wavelength (left) and pattern amplitude (right) as a function of the imposed frequency for (a) $\Gamma = 2.9$, (b) $\Gamma = 4$, (c) $\Gamma = 6$ (solid symbols are used to denote the numerically determined values, the solid spline is used to guide the eye, the curved dashed line indicates a c/f interpolating function where c is an ad-hoc constant, the uncertainties due to error measurements are as follows: 2% for panels (a) and (c), 4% for panel (b))

$f \leq 20$ Hz, the agreement with the c/f law is poor as another regime is met where the wavelength weakly depends on the frequency. Notably, the same trend for decreasing values of the frequency can also be identified in Fig. 5b, left panel, but it is no longer evident in Fig. 5c, which indicates that this regime is progressively shifted towards smaller frequencies as Γ grows.

3.2 Binary case

Having completed an analysis of the monodisperse case in terms of patterning behavior, wavelength and vertical extension, we turn now to the situation in which two different particle populations are present (that simply differ in regard to the diameters, namely, $d_1 = 1.6 \times 10^{-4}$ m and $d_2 = 8 \times 10^{-5}$ m, as indicated in Table 1). Although all the considered particles are still spherical and all made of the same material, this situation brings in two new degrees of freedom, namely, the total number of initial layers pertaining to the two different populations and the overall mass of the layer.

As a reduction in the number of parameters is always beneficial, in order to make a proper choice, in the following we rely on specific observations made by Bizon et al. [36].

These authors reported in the monodisperse case that the pattern wavelength is proportional to the layer depth, h and the effective driving frequency (which determines transitions between patterns at fixed Γ) is proportional to the square root of the layer depth [36]. Accordingly, in order to filter out possible effects due to variations induced by changes of h, we concentrate on a fundamental situation. More specifically, we examine circumstances for which the number of layers is such that the depth of the layer is the same and the total mass of the particles is approximately retained (this corresponding to a total of 9 layers, with 5 layers made of the large particles and the remaining 4 layers consisting of the small particles, i.e. $h = N_1 d_1 + N_2 d_2 = 5d_1 + 4d_2 = 1.12 \times 10^{-5}$ m).

At this stage, we wish to highlight that, for the sake of simplicity and brevity, although several simulations were conducted to investigate all these cases, in the following we focus on 3 representative situations in the space of parameters (Γ,f) only, namely, conditions for which in the monodisperse case, well-defined patterns with the square and hexagonal symmetry emerge. Moreover, for the square pattern, two different cases are analyzed, which relate to two different temporal responses of the system, i.e. $f/2$ and $f/4$.

Following a logical approach, we start with the case corresponding to a relatively small frequency and vibration amplitude, i.e. $f = 20$ Hz and $\Gamma = 2.9$ for which a well-defined square pattern with the $f/2$ temporal response was shown in Sect. 3.1. For the convenience of the reader, the original pattern is reported again in the present section to allow direct comparison with the bi-disperse case (Fig. 6a and b, respectively).

As a fleeting glimpse into Fig. 6 would immediately confirm, the major effect of the considered binary distribution of particles is a dramatic change in the topology of the waveform, which loses its original regular square organization. Surprisingly, as evident in Fig. 7, a triangular symmetry emerges at a certain stage (first panel). In particular, two characteristics stand out from this figure. The lines bounding the nodes (red peaks in the first panel of Fig. 7) give the observer the illusion of a very well-defined network resembling the typical architecture of reticular trusses. Moreover, a closer inspection of this figure reveals that most of these lines originate from a given point (highlighted using a black arrow). This point serves as a common vertex for many triangles. More specifically, it may be seen as the centre of a closed polygonal multi-cell structure having the shape of a "flower," with each triangular cell representing a distinct "petal". The above-mentioned special knot can be uniquely characterized through the topological order p of the radial spokes that originate from it (in practice it can be determined through analysis of the "angle" distribution as provided by the aforementioned Voronoi analysis [50, 51]). As evident in the first panel of Fig. 7, this topological order (p_{max} = maximum number of departing lines) is $p_{max} = 6$, whereas for the standard patterns with the classical hexagonal and square symmetry discussed in Sect. 3.1, p_{max} would take values $p_{max} = 3$ and $p_{max} = 4$, respectively.

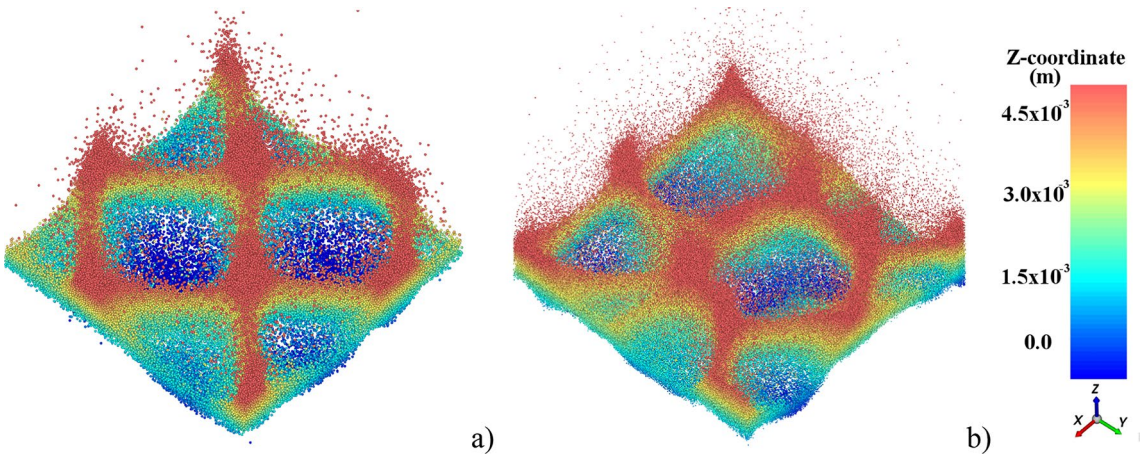

Fig. 6 Snapshots of 3D particle distribution in space for $\Gamma = 2.9$ and $f = 20$ Hz: (a) Monodisperse case ($N = 7$, $h = 7d_1 = 1.12 \times 10^{-5}$ m), (b) bi-disperse case ($N_{tot} = 9$, $h = 5d_1 + 4d_2 = 1.12 \times 10^{-5}$ m)

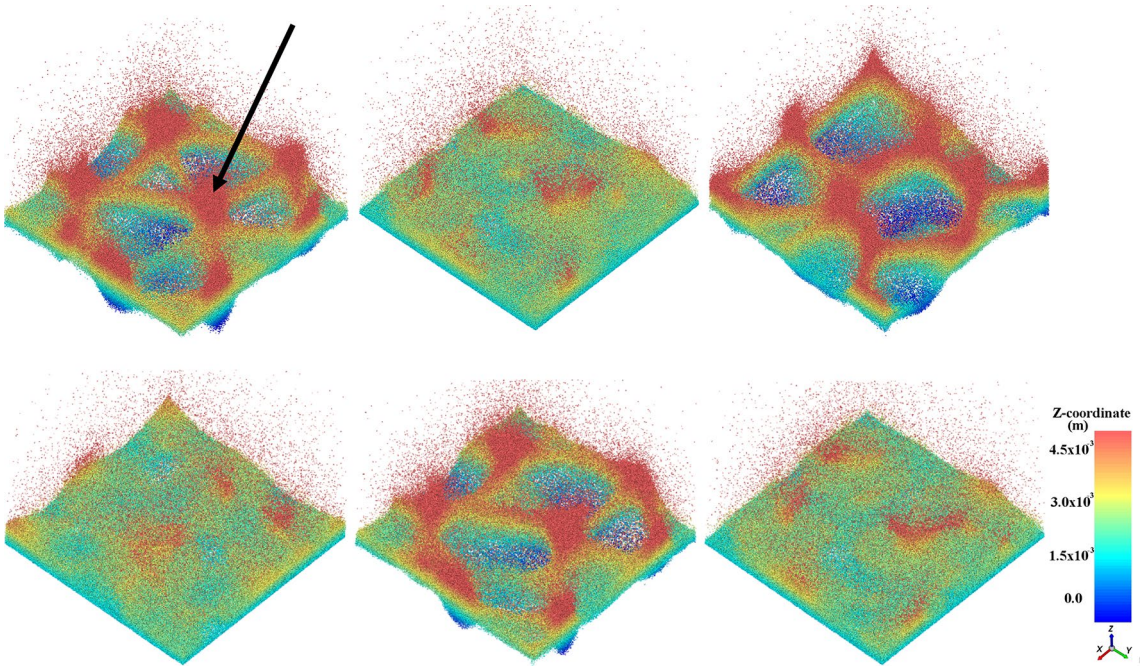

Fig. 7 Three-dimensional view of instantaneous particle distribution in space for $\Gamma = 2.9$ and $f = 20$ Hz in the bi-disperse case (N_{tot} =9, $h = 5d_1 + 4d_2 = 1.12 \times 10^{-5}$ m) at $t = t_0$, $t_0 + T/2$, $t_0 + T$, $t_0 + 3\ T/2$, $t_0 + 2\ T$, $t_0 + 5\ T/2$ where T is the period of externally imposed vibrations

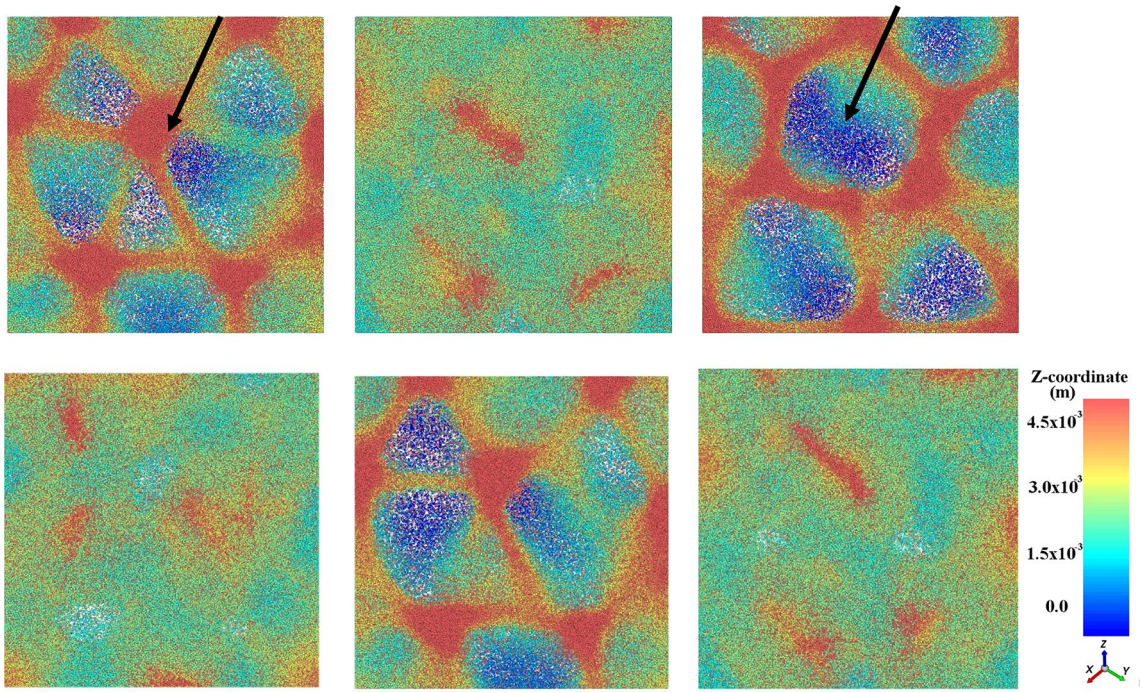

Fig. 8 Three-dimensional and top views of instantaneous particle distribution in space for $\Gamma = 2.9$ and $f = 20$ Hz in the bi-disperse case (N_{tot} =9, $h = 5d_1 + 4d_2 = 1.12 \times 10^{-5}$ m) at $t = t_0$, $t_0 + T/2$, $t_0 + T$, $t_0 + 3\ T/2$, $t_0 + 2\ T$, $t_0 + 5\ T/2$ where T is the period of externally imposed vibrations

Figure 7 is complemented by Fig. 8 where the evolution of the pattern over one period of vibrations can be clearly discerned. Taken together, both figures indicate that the triangular morphology is just a transient state, with a hexagonal pattern ($p_{max} = 3$) being attained ad the end of the vibration cycle, where the aforementioned point with topological order $p = 6$ is replaced by an antinode, i.e. the center of a hexagonal cell.

The next figure of the sequence (Fig. 9) refers to the case $\Gamma = 4$ and $f = 40$ Hz for which the pattern in the monodisperse was formed by regular hexagons (Fig. 9a).

At first glance, the second panel for the binary case with $N_{tot} = 9$ (shown in Fig. 9b), indicates that a variation in the particle size distribution has no impact on the emerging waveform, which retains the hexagonal symmetry in all cases. The same concept applies to the wavelength (the variations are minimal). However, upon closer analysis, these cases have been found to display interesting differences in terms of micro-mechanical behaviors (we will discuss these aspects in Sect. 3.6).

Moving on to the case $\Gamma = 6$ and $f = 60$ Hz, Fig. 10 provides good impression of the three-dimensional motion once again in the two fundamental situations considered previously (monodisperse case with $N = 7$, binary case with $N_{tot} = 9$, respectively).

By visual inspection of this figure, the reader will realize that a binary distribution of particles can lead to a degradation of the original perfect symmetry obtained in the monodisperse case. Direct comparison of the cases with equivalent depth (i.e. Figure 10a with respect to Fig. 10b) is meaningful as it shows that there is a tendency to replace an ordered arrangement of squares with a less regular pattern featuring stripes.

3.3 Ternary case

In this section, we lend our attention to the situation in which three distinct particle sizes are present at the same time, namely, 1.6×10^{-4} m, 1.2×10^{-4} m and 8×10^{-5} m (see again Table 1). By analogy with the approach already undertaken in the bi-disperse case, we limit ourselves to considering a particle distribution for which the same layer depth is approximately retained (a condition achieved by assuming 3 layers for each particle size $N_1 = N_2 = N_3 = 3 \rightarrow h = N_1 d_1 + N_2 d_2 + N_3 d_3 = 1.08 \times 10^{-5}$ m, which differs by only 3% with respect to the monodisperse case, Figs. 11, 12 and 13).

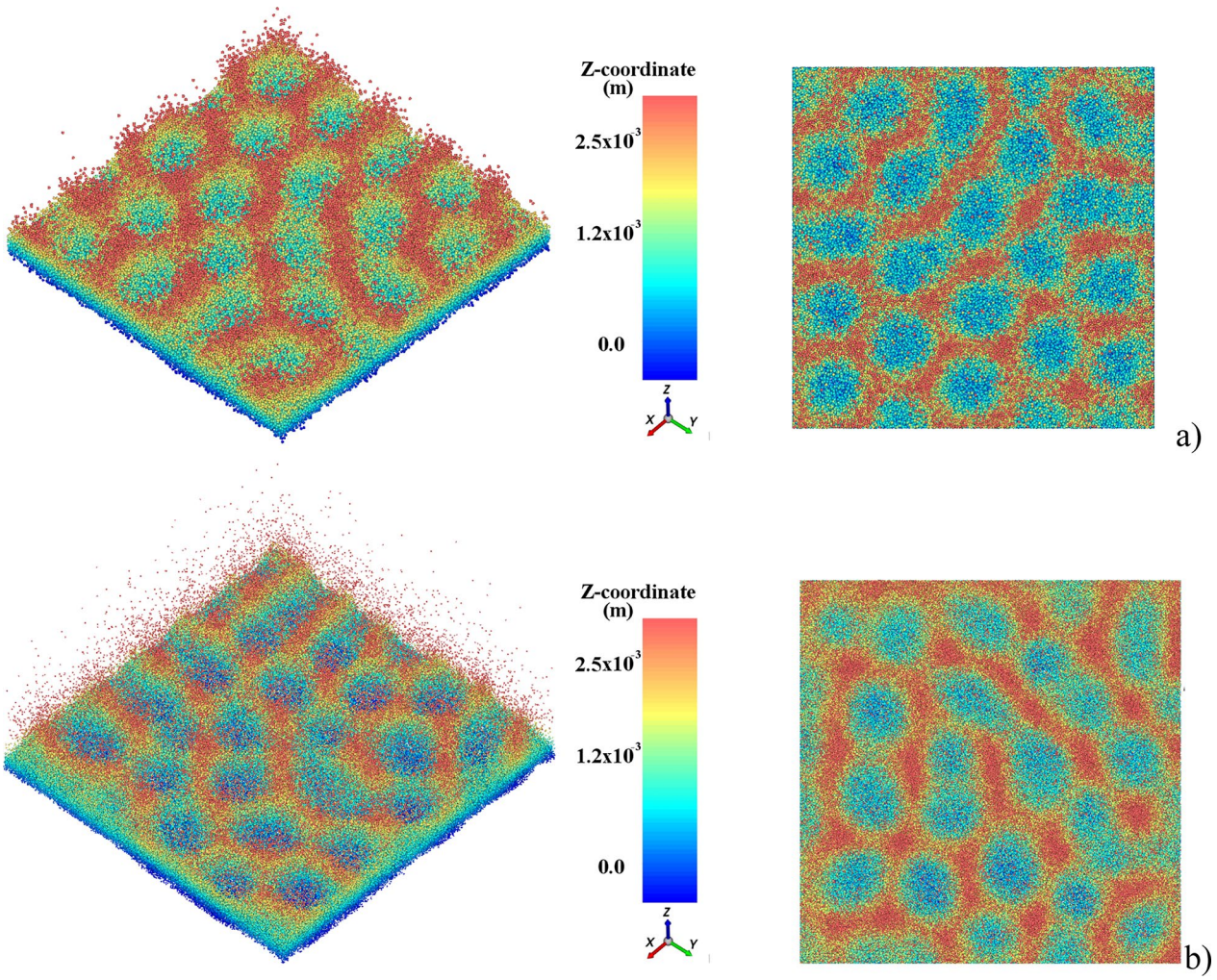

Fig. 9 Instantaneous particle distribution for $\Gamma = 4$ and $f = 40$ Hz: (a) monodisperse case, (b) bi-disperse case with $N_{tot} = 9$

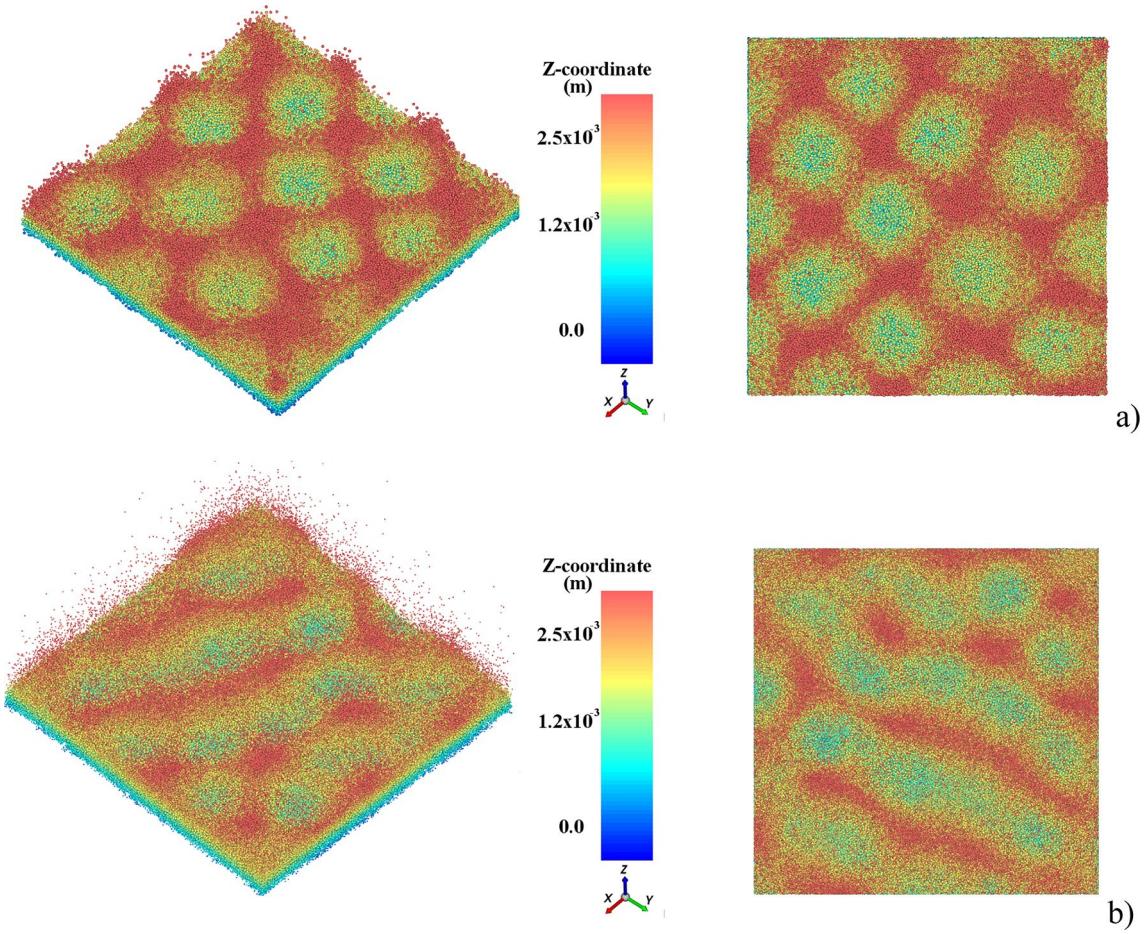

Fig. 10 Instantaneous particle distribution for $\Gamma = 6$ and $f = 60$ Hz: (a) monodisperse case, (b) bi-disperse case with $N_{tot} = 9$

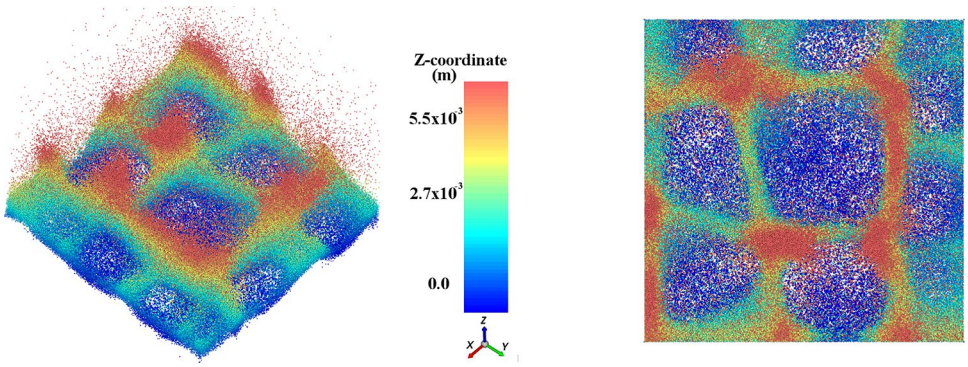

Fig. 11 Three-dimensional (left) and top (right) views of instantaneous particle distribution in space for $\Gamma = 2.9$ and $f = 20$ Hz in the ternary case

The significance of these additional figures resides in their ability to make evident that an increase in the number of different sizes with which particles are present in the material yet adds complexity to the problem. It causes a variation in the patterning behavior and related quantitative metrics. Indeed, a consistent decrease can be spotted in the pattern wavelength, which displays in general a small but yet appreciable variation when moving from the situation with one particle size to those with two and three particle populations. Much more evident changes, however, concern the pattern. While for $\Gamma = 4$ and $f = 40$ Hz, a disordered distribution of pentagons and four-side polygons was obtained, for $\Gamma = 2.9$ and $f = 20$ Hz, the perfectly square and triangular/hexagonal waveforms seen for monodisperse and two-disperse particle distributions, respectively, are taken over by a set of irregular polygons with three or four sides. The modifications showing up for $\Gamma = 6$ and $f = 60$ are even more dramatic; the perfect arrangement of squares found in the monodisperse case, which for a binary distribution of particles was replaced by a combination of squares and stripes,

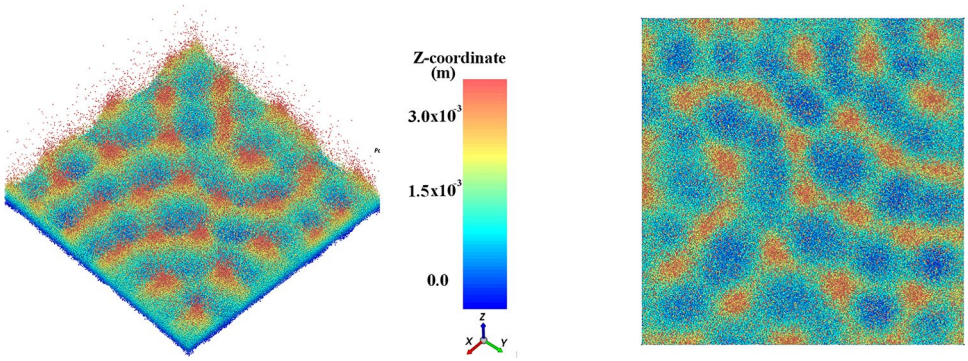

Fig. 12 Three-dimensional (left), top (right) views of instantaneous particle distribution in space for $\Gamma = 4$ and $f = 40$ Hz in the ternary case

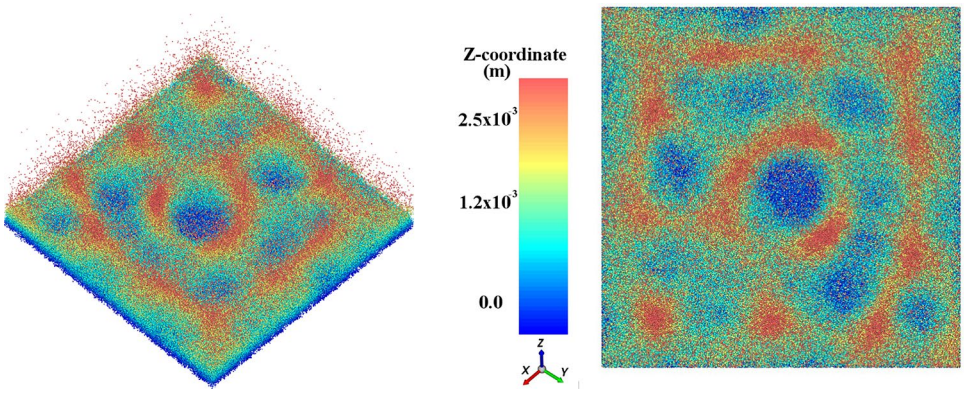

Fig. 13 Three-dimensional (left), top (right) views of instantaneous particle distribution in space for $\Gamma = 6$ and $f = 60$ Hz in the ternary case

is taken over by a new configurations with a larger central feature, resembling a crater and having an incommensurable wavelength.

3.4 Voronoi Analysis for multi-disperse cases

In this section, the progressive corrugation of the pattern seen for $\Gamma = 4$ and $f = 40$ Hz (transitioning from a perfect distribution of hexagons to a disordered mixture of pentagons and four-side polygons) is further explored quantitatively by means of the aforementioned Voronoi analysis [50, 51], by which a variety of details concerning the geometrical nature of the pattern can be obtained. The outcomes of this analysis for such a representative case are summarized in Fig. 14; and Table 5.

Interestingly, it can be seen that on increasing the number of particle sizes, the average angle becomes progressively higher, which indirectly witnesses the emergence of polygons with a smaller number of sides. As this occurs in conjunction with a small decrease in the pattern wavelength, this initially leads to an increase in the number of cells (17 in the binary case as opposed to 13 in the monodisperse distribution). However, this tendency is mitigated by the emergence of a larger number of squares and pentagons in the ternary case, which causes a decrease in the cell number.

For the sake of completeness, Fig. 15 shows the corresponding analysis for the ternary system and $\Gamma = 6, f = 60$ Hz for which only square cells had been obtained in the monodisperse case.

3.5 Segregation effects

The results discussed in the preceding sections are further complemented by an analysis of segregation effects, as shown in Figs. 16, 17, 18, and 19, 20, 21 for the binary and ternary cases, respectively.

In these figures, different colors have been used to reveal the position of particles with different size throughout a vibration cycle. They are interesting as some commonalities can be revealed for both the binary and ternary cases in terms of particle size distribution.

In particular, in the binary cases, regardless of the considered frequency, Γ and related emerging pattern, a kind of three-layered structure can be recognized, with an extremely thin layer of small particles (8×10^{-5} m) located at the bottom (blue color), an intermediate layer essentially made of larger particles (red color) and a top layer made again of small particles, but with particle volume fraction gradually decreasing towards the top (as opposed to the bottom layer where the transition from the granular material to underlying space is abrupt).

When three particle populations are considered, the dynamics are essentially the same. A thin bottom and an upper layer of blue (small particles) can be still recognized. A central layer also exists, but no segregation seems to affect

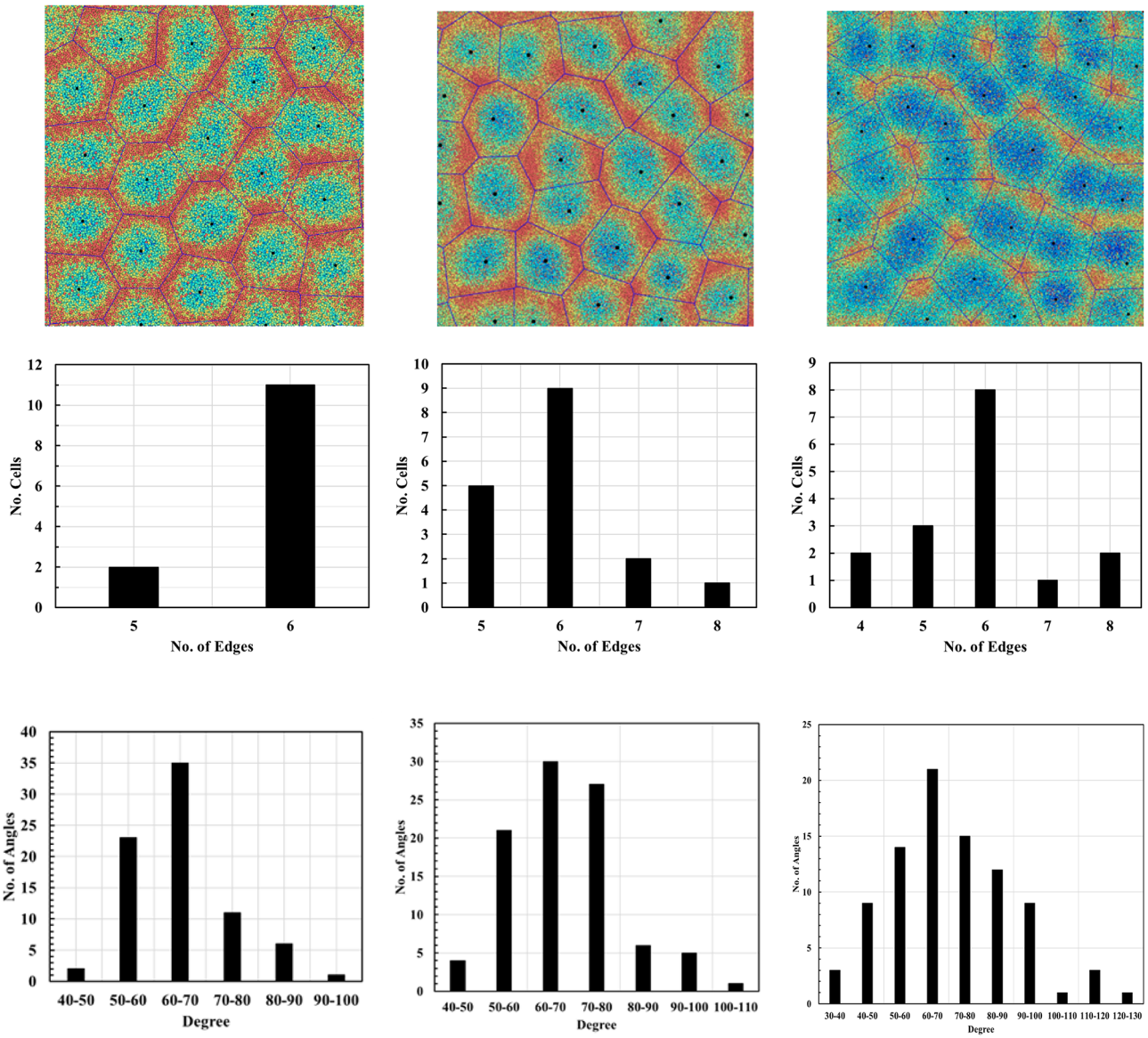

Fig. 14 Outcomes of Voronoi analysis for $\Gamma = 4$ and $f = 40$ Hz in the monodisperse (first column), binary (second column) and ternary (third column) case. The first row shows the node connecting lines as identified through the tessellation analysis, the second and third rows provide the related edge and angle distributions, respectively

Table 5 Outcomes of Voronoi analysis for the $\Gamma = 4$ and $f = 40$ Hz in the monodisperse and polydisperse cases

Dispersity	Total no. of angles	Mean angle size (°)	Total no. of cells
Mono	78	64.53	13
Bi	94	67.65	17
Tri	88	69.94	16

the particles with intermediate and large sizes (1.2×10^{-4} m and 1.6×10^{-4} m). These cluster forming a band that constitutes the "core" of the bed and retains an almost uniform degree of mixing throughout the process. Although these phenomena would deserve a study on their own given the complexity and variety of phenomena that can cause layer stratification in vibrated isodense granular materials [54–56], here we limit ourselves to mentioning that the inability of the ternary case to display further stratification (i.e. the formation of extra layers) should be sought in the reduced particle size difference in this case concerning the intermeadiate and larger particles (1.6×10^{-4} / 1.2×10^{-4} =1.3 for the green and red particles in Figs. 19, 20 and 21 as opposed to 1.6×10^{-4} / 8×10^{-5} =2 for the small and large particles in Figs. 16, 17 and 18). Indeed, a significant body of research supports the idea that a smaller difference

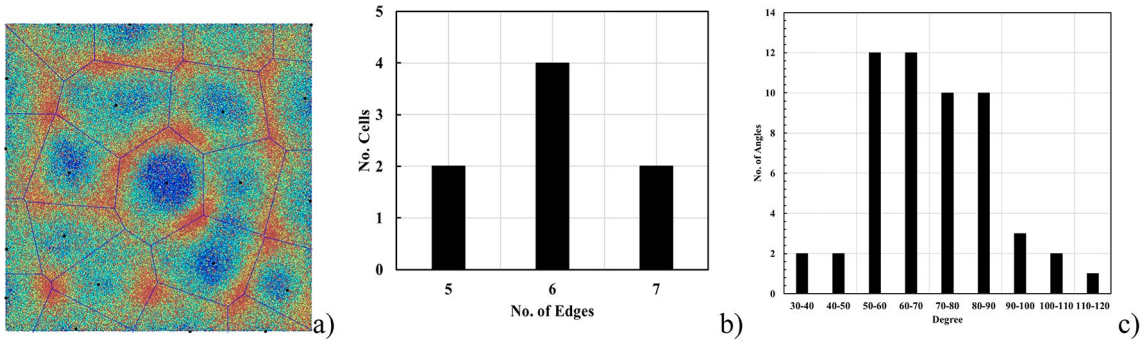

Fig. 15 Outcomes of Voronoi analysis for $\Gamma = 6$ and $f = 60$ Hz in the ternary case

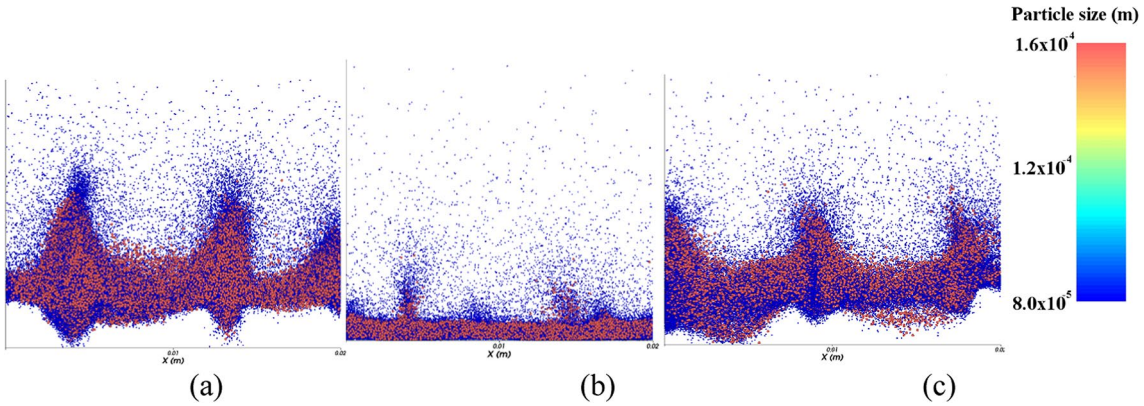

Fig. 16 Side views of 3D particle size distribution in space for $\Gamma = 2.9$ and $f = 20$ Hz in the bi-disperse case at (a) $t = t_0$, (b) $t_0 + T/2$, (c) $t_0 + T$

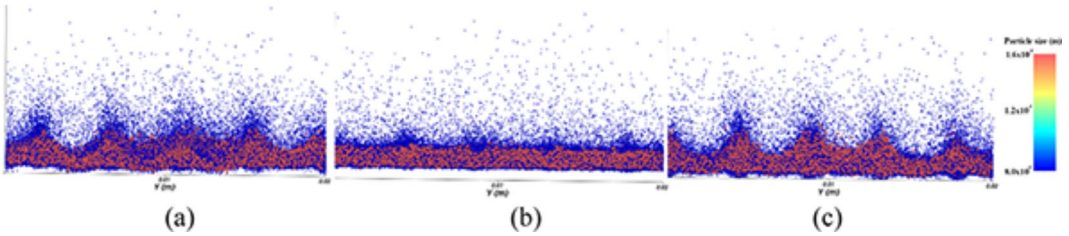

Fig. 17 Side views of 3D particle size distribution in space for $\Gamma = 4$ and $f = 40$ Hz in the bi-disperse case at (a) $t = t_0$, (b) $t_0 + T/2$, (c) $t_0 + T$.

in particle size decreases the likelihood of stratification in granular materials [57].

Figures 19 and 20 are useful also for another reason. It is evident there that the vertical distance or separation of the nodes from the antinodes tends to decrease in the middle of a vibration cycle, with the particle size distribution staying relatively consistent throughout. Figure 21 however indicates that in the $\Gamma = 6$ and $f = 60$ Hz case, a well-defined pattern (with large vertical amplitude) is only effectively generated every two vibration periods (we will provide additional information about this behavior in Sect. 3.6). Further assessment of Figs. 19 and 20 with respect to Fig. 21 also leads to the conclusion that while the core layer made of medium and largest particles is deformed in correspondence of the peaks for $\Gamma = 2.9$ and $\Gamma = 4$, it is flattened for $\Gamma = 6$, with the smallest particles only contributing to the formation of the nodes (peaks).

3.6 Power Spectra, Dissipation and Collision statistics

This section is finally devoted to a discussion of the additional insights into these dynamics, which stem from an analysis of the additional quantities introduced in Sect. 2.3.

In particular, we start from a description of the number of collisions occurring among all involved particles as a function of time. In this regard, a first key observation stemming from Fig. 22 concerns the evident analogy existing between the different cases. Regardless of the considered values of frequency and Γ, a similar trend can be identified in terms of

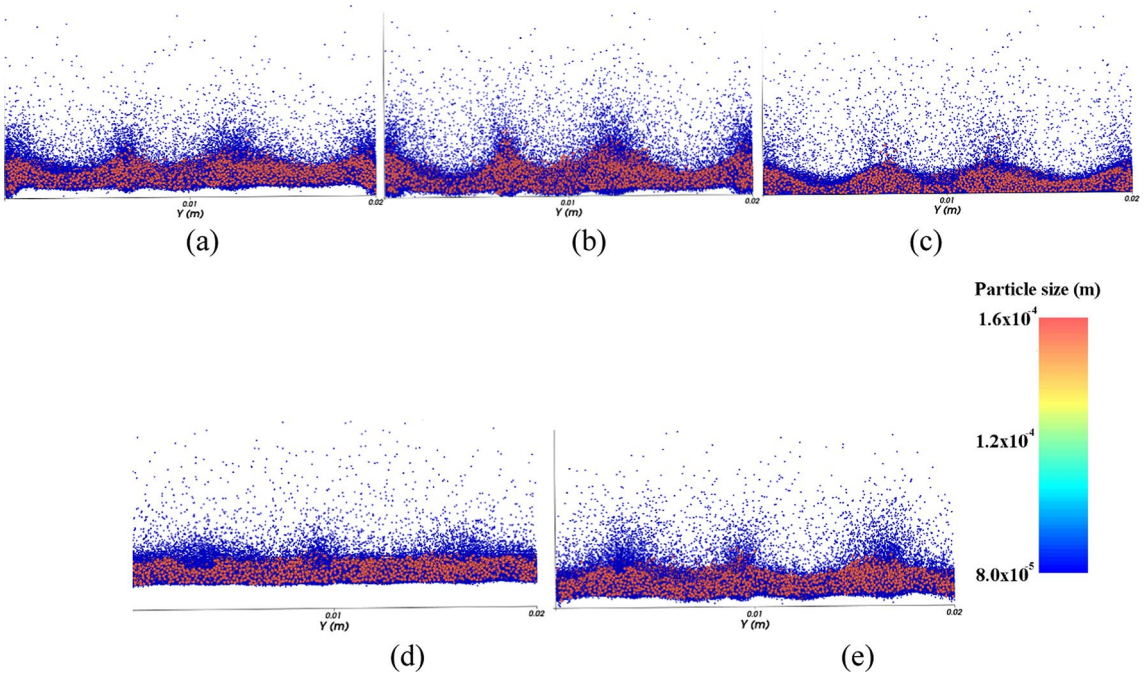

Fig. 18 side views of 3D particle size distribution in space for $\Gamma = 6$ and $f = 60$ Hz in the bi-disperse case at (a) $t = t_0$, (b) $t_0 + T/2$, (c) $t_0 + T$, (d) $t_0 + 3T/2$, (e) $t_0 + 2T$

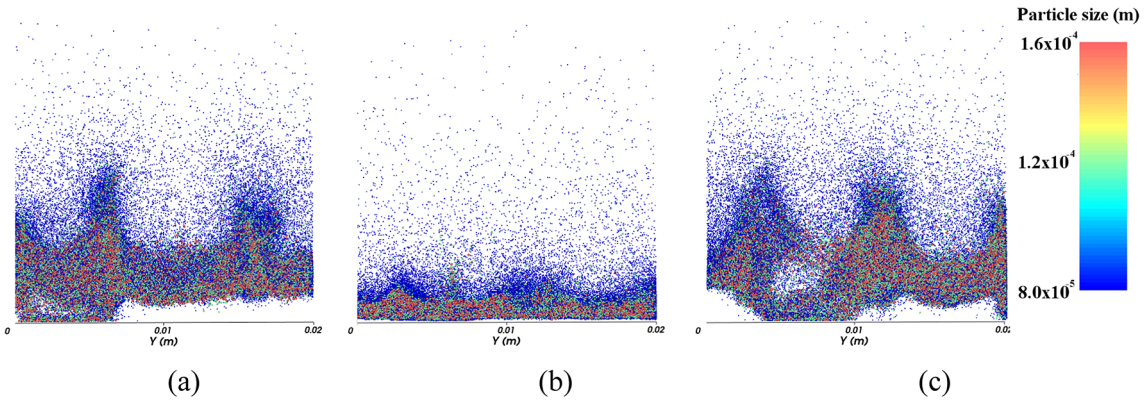

Fig. 19 Side views of 3D particle size distribution in space for $\Gamma = 2.9$ and $f = 20$ Hz in the ternary case at (a) $t = t_0$, (b) $t_0 + T/2$, (c) $t_0 + T$

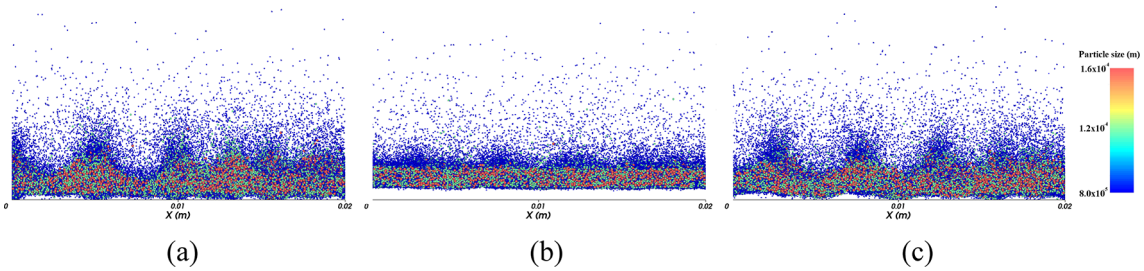

Fig. 20 Side views of 3D particle size distribution in space for $\Gamma = 4$ and $f = 40$ Hz in the ternary case at (a) $t = t_0$, (b) $t_0 + T/2$, (c) $t_0 + T$

collision statistics. In particular, the highest number of collisions occurs in the ternary and the binary cases.

Although a simplistic justification of this behavior could be directly routed in the higher number (n_{tot}) of particles being involved in the multi-disperse cases (One-size – $n_{mono} = 107632$, $d = 1.6 \times 10^{-4}$ m, Two-size $N = 9$ – $n_{totbinary} = 324844$, $d_{average} \cong 9.89 \times 10^{-5}$, 3size – $n_{totternary} = 314456$, $d_{average} \cong 1.02 \times 10^{-4}$), consideration of Figs. 22 and 23

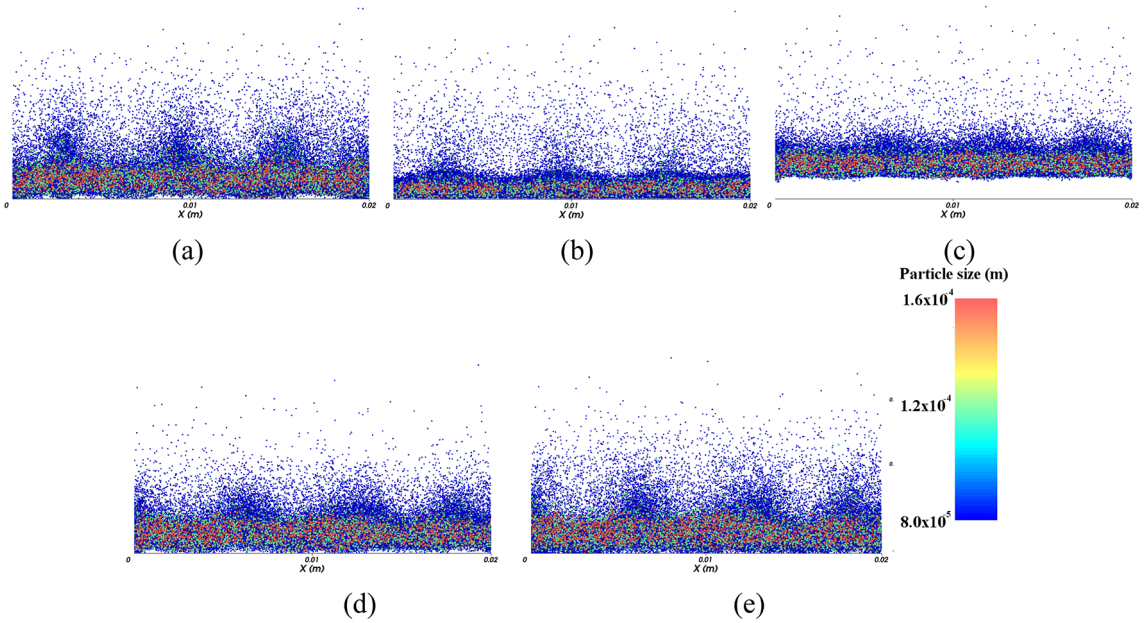

Fig. 21 side views of 3D particle size distribution in space for $\Gamma = 6$ and $f = 60$ Hz in the ternary case at (a) $t = t_0$, (b) $t_0 + T/2$, (c) $t_0 + T$, (d) $t_0 + 3T/2$, (e) $t_0 + 2T$

clearly indicates that the specific composition of the mixture and the topology of the pattern does also play a significant role.

In this regard first it is instructive to take a look at Fig. 23a where the percentage increase (*delta with respect to the monodisperse case*) of the average collision frequency peak has been plotted as a function of the total number of particles for the binary and ternary cases. This figure clearly shows that although an increase in the number of particles from the monodisperse (n_{mono}) to the ternary distribution ($n_{ternary}$) obviously causes a large increase in the frequency peak ($\cong$ 58%, 130% and 40% for Fig. 22a, b and c, respectively), however, a further increase in the particle number ($n_{binary} > n_{ternary}$) does not produce higher peaks (as made evident by the decreasing trends shown in Fig. 23a).

As outlined above, the pattern does play an even more substantial role. When the original waveform in the monodisperse case consists of hexagons ($\Gamma = 4$ and $f = 40$ Hz) and, accordingly, the number of radial spokes originating from nodes is $p = 3$, a maximum is obtained in the percentage increase (the green line in Fig. 23 is always located above all the other lines). However, this percentage undergoes a notable decrease in the situations where the dominant pattern is characterized by a topological order $p > 3$ (namely the patterns with the square, triangular or hybrid symmetry shown in Figs. 6a, 7 and 10, corresponding to the black and brown lines in Fig. 23).

Elaborating a physical interpretation for all these connections is obviously a very difficult task due to the highly non-linear nature of the underlying cause-and-effect relationships. Anyhow, in the following another attempt is made to distillate out some common trends by looking at quantities more directly involved in the pattern formation mechanisms.

4 Discussion

As already explained to a certain extent in the introduction, order in complex systems generally emerges essentially as a result of a mechanism by which the *energy available at large scales* is redistributed or reorganized over different spatial and/or temporal scales until it is "*dissipated*" at a microscopic level. By putting *a limit to the minimum self-organization scale* in the system, dissipation is therefore expected to play an important role in such a process.

Once again, an analogy with corresponding fluid-dynamic behaviors may help to present such concepts with a more clear perspective. As a term of comparison, in particular, we consider the development of fluid convection in fluids uniformly heated from below and cooled from above (the so-called Rayleigh-Bénard convection). This fluid-dynamic problem has been extensively investigated in the literature given its fundamental nature and involvement in a number of natural and technological processes [25]. It is known that the dynamics of such systems are essentially driven by a balance of forces, namely, the buoyancy force produced by the thermal energy injected into the system at a large scale (due to the application of a temperature gradient and the presence of gravity) and the viscous forces opposing

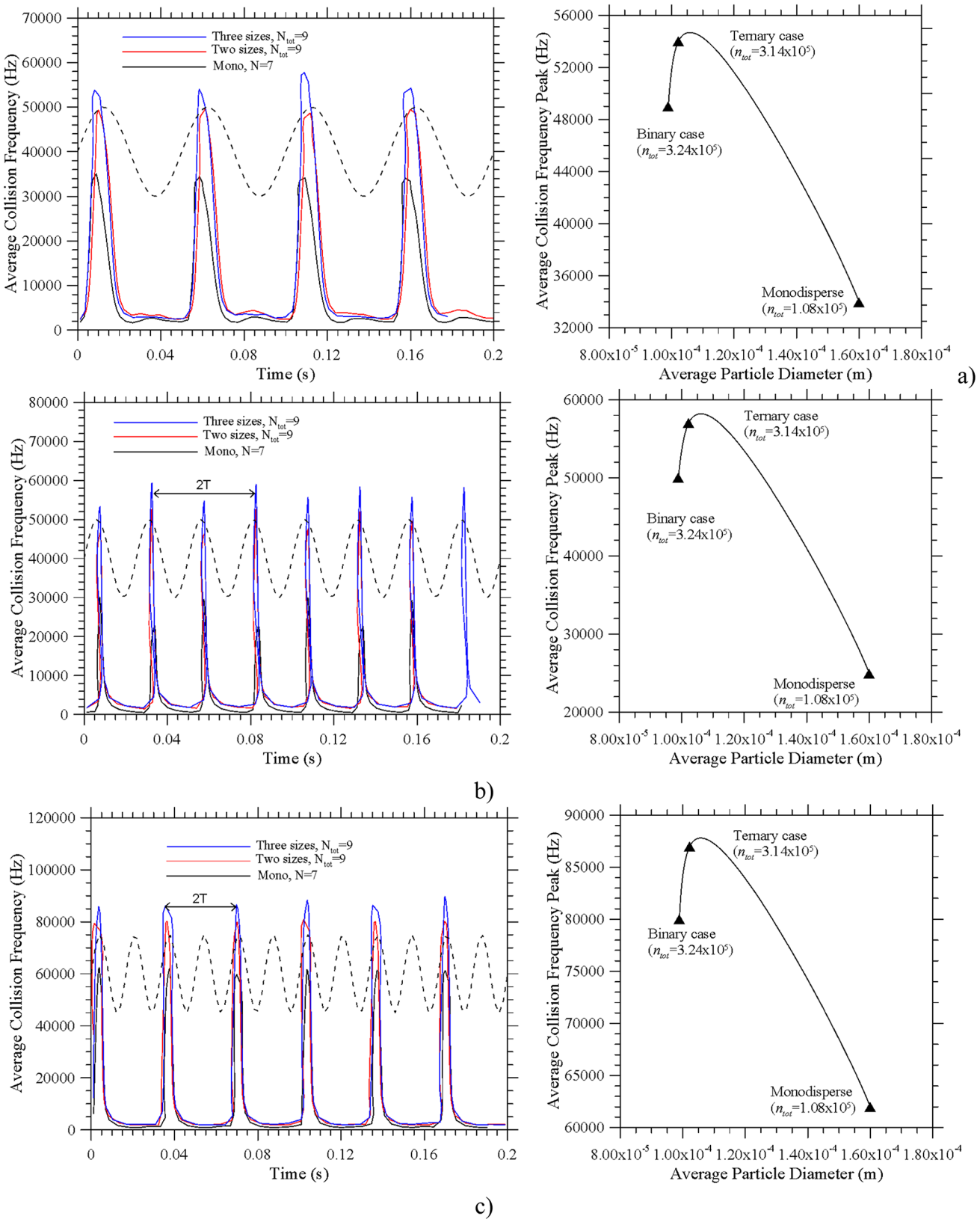

Fig. 22 Collision statistics for (a) $\Gamma = 2.9$ and $f = 20$ Hz, (b) $\Gamma = 4$ and $f = 40$ Hz, (c) $\Gamma = 6$ and $f = 60$ Hz (the dashed black line qualitatively indicates the forcing, i.e. the time-varying acceleration due to the imposed vibrations; n_{tot} indicates the total number of particles in the domain)

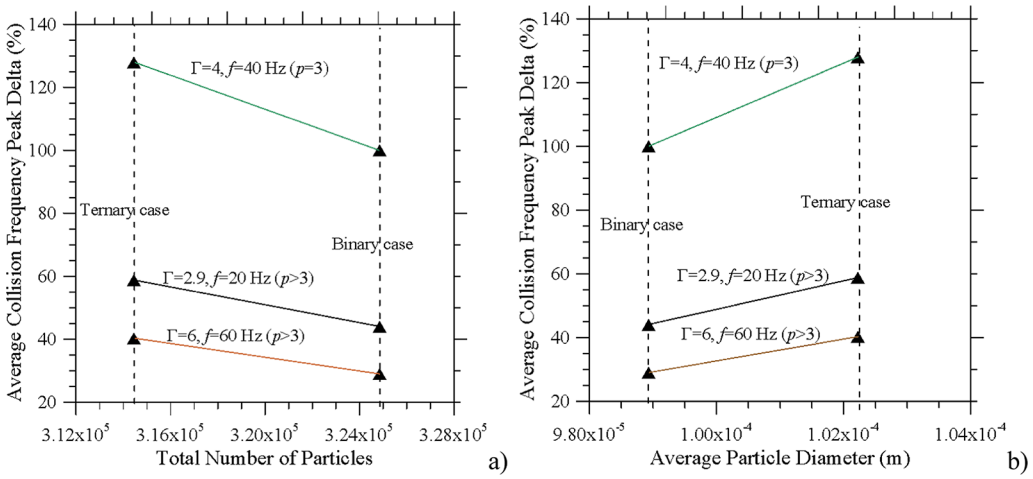

Fig. 23 Percentage increase (*delta with respect to the monodisperse case*) of the average collision frequency peak for the same conditions considered in Fig. 22: (a) delta as a function of the total number of particles, (b) delta as a function of the average particle diameter defined as $d_{mean} = (n_1 d_1 + n_2 d_2 + n_3 d_3)/n_{tot}$ where n_i indicates the number of particles for each size and n_{tot} the total number of particles in the domain

motion. On increasing the former (or decreasing the latter), Rayleigh-Bénard convection generally evolves towards situations where the *typical pattern wavelength decreases* (i.e. higher wavenumbers are excited) because the scale at which the energy is completely dissipated becomes progressively smaller (under a slightly different perspective one may say, that on increasing the macroscopic energy level, energy is able to flow *over a larger number of scales*). No further flow spatial features can be produced for scales smaller than the dissipation scale, as no energy is available to do so.

This process finds its ultimate verification in the so-called Kolmogorov theory [58–61] for isotropic turbulence according to which, vortices present in the considered flow can contain vortices of smaller size, which in turn contain even smaller vortices and this process can be iterated in space until a scale is reached where the kinetic energy (continuously transferred from large scales to smaller scales) is finally dissipated (Kolmogorov length scale). The Kolmogorov length represents the size of the smallest "eddies" present in the flow.

Analogous arguments might be used for the problem considered in this work to interpret the observed trends in terms of wavelength. Obviously, some important differences exist with respect to the companion situation in which the considered material is a real fluid because solid particles or grains dissipate energy through other mechanisms. More specifically, in addition to dissipation due to frictional stresses, kinetic energy is transformed into internal energy due to the inelastic nature of the particles or grains themselves. Nevertheless, some consensus exists (see, e.g., Taguchi [62] and Radjai and Roux [63]) that arguments valid for fluids might be translated to granular materials because these have often been observed to follow the Kolmogorov theory. Although inertia governs the energy cascade in Newtonian fluids, whereas in granular materials it also depends on the geometrical compatibility of the strain with particle arrangements, as a matter of fact, granular flows often obey laws identical to that originally predicted by Kolmogorov [25].

Building on such analogy, the trends in terms of *total dissipated power* recognizable in Fig. 24 (left panel) are therefore consistent with the small (but non-negligible) decrease in the pattern wavelength seen when the number of particle sizes is progressively increased from 1 to 3. The peaks of total dissipated power gradually increase on moving from the monodisperse case to those with two and three particle sizes and the same layer depth and, accordingly, the pattern wavelength undergoes an appreciable shrinkage.

Additional insights follow naturally from a comparison of the left (total) and right (average) power. All these plots account essentially for the power dissipated due to the inelastic nature of the collisions occurring between particles. When the average values defined through Eq. (20) are considered (right panels), it can be seen (as expected) that the maximum dissipation (per particle) is obtained in the monodisperse case for which all the particles have a relatively large size (and accordingly a larger volume from which the larger dissipation resulting from inelastic collisions). When smaller particles enter the dynamics (and the overall number of particles increases in order to retain the same system mass), the average dissipation per particle undergoes a shrinkage owing to two concurrent effects, namely, the larger number of particles (leading to a higher value at the denominator of Eq. (20)) and the smaller volume that can contribute to inelastic dissipation according to the mechanism described in Sect. 2.2.

As already noted for the collision statistics, the situation in which the dominant pattern is the hexagonal one (green lines in Fig. 24a) deserves some additional attention.

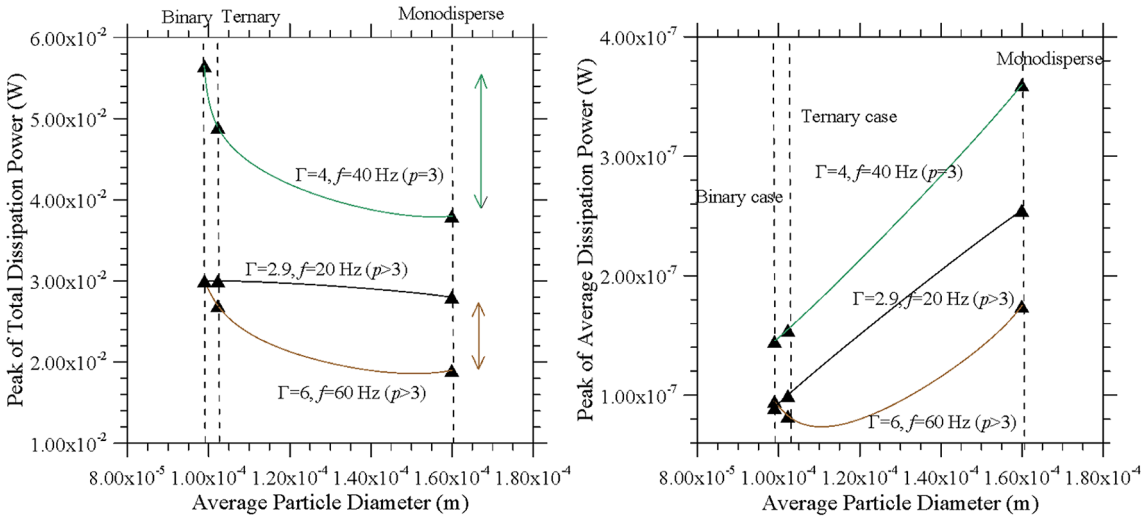

Fig. 24 Total (left) and average (right) dissipated power peaks versus the average particle size

In this case, the increase in the peaks of dissipated power (with respect to the monodisperse situation) is the highest, which once again witnesses the inter-relatedness of the pattern specific topological configuration and the way by which the vibrational energy injected at large scale into the system is used to produce kinetic energy or dissipated. When the convective cells have the shape of hexagons, the binary and ternary granular materials display an increased ability to dissipate energy with respect to the corresponding monodisperse situation. Notably, this occurs in conjunction with the observed *higher stability* of the hexagonal pattern, which does not undergo significant topological modifications in the multi-disperse configurations. Interestingly, this may represent an additional hint for the elaboration of a relevant analogy with fluid-dynamic systems, in particular, again with the aforementioned Rayleigh-Bénard convection problem. Indeed, it is known that in specific conditions, this convective system, which in general displays simple two-dimensional rolls as the preferred form of convection over a wide region of the space of parameters, can produce hexagonal cells. In particular, this happens when the reflectional symmetry is violated [64–66] i.e. when physical effects exist that break the up-down system invariance. As this also happens in the present case (see again Fig. 20) due to the tendency of the larger particles to form a (vertical-symmetry-breaking) cohesive layer under the effect of vibrations, this might be seen as a clue for a possible role of such an effect in the present situation.

Although the arguments elaborated before about the increase in dissipation in certain cases align with the observed slight decrease in the wavelength of the pattern and might be used to infer a physical interpretation for such a trend, however, it should be pointed out that granular materials are not perfectly equivalent to Newtonian fluids. As already outlined in the introduction, the stress tensor for granular materials can be generally seen as the combination (mathematical summation) of two different contributions, one accounting for the stresses due to the contact forces represented by Eq. (8) and another term related to inertial effects (particle acceleration, which by means of mathematical manipulations can be expressed as a function of the particle translational and rotational velocity [25, 30, 31]).

Notably, while this part is similar to that for Newtonian liquids (as it involves kinematic quantities only), thereby setting an analogy between granular materials and Newtonian liquids, the other contact-force-related term might be seen as an analogue (from a certain point of view) of the extra stress tensor for a viscoelastic fluid. This leads to another line of reasoning [67–69] in principle allowing additional insights into the considered phenomena to be sought through comparison with patterning behavior in *viscoelastic fluids*. As an example, referring for simplicity once again to the case of natural convection where the temperature gradient is vertical (just as vibrations considered in the present study), the reader may consider Lappa and Ferialdi [70]. These authors observed that, starting from a situation where the so-called Marangoni-Bénard convection displays a very regular pattern (Newtonian fluid case), a progressive corrugation of the otherwise perfective arrangement of convective cells could be obtained by increasing the level of fluid elasticity, i.e. by making the relative importance of the additional stress due to elastic forces increasingly higher with respect to that related to the gradient of macroscopic velocity. Most remarkably, in perfect analogy with the present findings, the corrugation showed up as a progressive increase in the number of pattern defects and an ensuing change in the shape of the convective cells (evolving from a set of identical items to a distribution of irregular polygons

with a varying non spatially-uniform number of sides). Oscillons were also found to emerge in specific situations.

Given the non-perfectly elastic behavior of such forces in the case of granular materials, pursuing further the analogy with viscoelastic fluids is not possible. Nevertheless, this line of thinking clearly points towards the potential role played by collisional stresses in determining the corrugation of the monodisperse pattern when multi-disperse distributions are considered. This argument is indeed supported by the realization that the peaks of total power globally dissipated through inelastic collisions grows when moving from the monodisperse to multi-disperse situations (see again the left panel of Fig. 24).

5 Conclusions

The regular and less regular waveforms produced by the application of vertical vibrational forcing to a granular material have been investigated for increasing levels of complexity due to a systematic variation in the size of the particles. Starting from the canonical situation in which all the grains have the same size, the initial situation has been progressively perturbed by changing the size of a given percentage of particles while retaining the same layer depth.

The results have revealed a kaleidoscope of situations with patterns readily switching among multiple morphologies on changing the amplitude and/or frequency of imposed vibrations. This process is mediated by the material composition. Even if all the particles have the same density and therefore no mixing can be induced due to density effects, an increase in the number of involved sizes generally leads to a corrugation in the (otherwise) perfect topology of the pattern, which somehow resembles that observed in earlier studies dealing with natural convection in viscoelastic fluids. For a fixed initial mass, a reduction in the pattern wavelength can be generally induced by acting on three distinct parameters, namely, the frequency of vibrations, the amplitude of the ensuing acceleration and particle size distribution.

In terms of morphology, hexagonal patterns seem to be much more stable as they exist over a larger range of frequencies and are weakly affected by a change in the particle-size distribution. In these conditions, the increase in the energy dissipated (peak) induced by the multi-disperse nature of the material attains a maximum with respect to other pattern morphologies. Patterns with the square symmetry are much more sensitive to a variation in the particle size distribution and are generally replaced by more chaotic configurations. However, specific circumstances also exist ($\Gamma = 2.9$, $f = 20$ Hz and binary case) where the initial square morphology evolves into a completely new, yet very regular, topology featuring triangular convective cells and a topological order (p_{max} = maximum number of departing lines) as high as $p_{max} = 6$ in some regions of the domain at specific times during the vibrational cycle.

Critical comparison with existing knowledge indicates that while some features might be interpreted on the basis of energy considerations derived from theories valid in the case of Newtonian fluids, other aspects require microphysical reasoning about the specific stresses at play in the considered problem. Future work shall be devoted to delving into these mechanisms. Although adequate mathematical models are not available yet, and the exact processes driving pattern formation in granular materials still represent a conundrum, the results described in this work have been presented under the optimistic hope that the related trends may serve as a basis for future developments.

Acknowledgements The authors would like to thank the NVIDIA Applied Research Accelerator program support and the CADFEM UK for Rocky license and support.

Author contributions P.W. conducted the required numerical simulations and prepared all the figures showing the particle distribution.S.V.B. contributed to the literature review and to the supervision of P.W. A.A. contributed to the description of the mathematical model. M.L. (P.W. supervisor) interpreted the results in the light of existing literature, elaborated relevant analogies with other non-linear systems and wrote the main manuscript text. All authors reviewed the manuscript.

Funding This work has been financially supported by the European Space Agency, ESA Contract 4000138607/22/NL/GLC/my, the Open Space Innovation Platform (OSIP). The authors wish to acknowledge also the support of EPSRC for contributing to the PhD scholarship of P. Watson.

Data availability The data that support the findings of this study are openly available in Pure, at https://doi.org/10.15129/f661d25d-9ae4-49f9-b140-bfbbe255e1ca.

Declarations

Conflict of interest The authors declare no competing interests.

References

1. Shevtsova, V., Mialdun, A., Melnikov, D., Ryzhkov, I., Gaponenko, Y., Saghir, Z., Lyubimova, T., Legros, J.C.: The IVIDIL experiment onboard the ISS: Thermodiffusion in the presence of controlled vibrations. Comptes Rendus Mécanique **339**(5), 310–317 (2011)
2. Lyubimova, T., Kovalevskaya, K.: Gravity modulation effect on the onset of thermal buoyancy convection in a horizontal layer of the Oldroyd fluid. Fluid Dyn. Res. **48**, 061419 (2016)
3. Vorobev, A., Lyubimova, T.P.: Vibrational convection in a heterogeneous binary mixture. Part 1. Time-averaged equations. J. Fluid Mech. **870**, 543 (2019)
4. Jefferies, M., Been, K.: Soil Liquefaction: A Critical State Approach, 2nd ed (CRC Press, 2016)
5. Yasui, M., Matsumoto, E., Arakawa, M.: Experimental study on impact-induced seismic wave propagation through granular materials. Icarus **260**, 320–331 (2015)
6. Reffet, E., Du Pont, S.C., Hersen, P., Douady, S.: Formation and stability of transverse and longitudinal sand dunes. Geology **38**(6), 491–494 (2010)
7. Parsons, A.J., Wainwright, J., Mark Powell, D., Kaduk, J., Brazier, R.E.: A conceptual model for determining soil erosion by water. Earth Surf. Process. Landforms **29**(10), 1293–1302 (2004)
8. Hyodo, R., Kurosawa, K., Genda, H., Kurosawa, K.: Transport of impact ejecta from Mars to its moons as a means to reveal Martian history. Sci. Rep. **9**, 19833 (2019)
9. Sonnergaard, J.M.: Quantification of the compactibility of pharmaceutical powders. Eur. J. Pharm. Biopharm. **63**(3), 270–277 (2006)
10. Ketterhagen, W.R., am Ende, M.T. and Hancock, B.C.: Process modeling in the pharmaceutical industry using the discrete element method. J. Pharm. Sci. **98**(2), 442–470 (2009)
11. Cante, J.C., Riera, M.D., Oliver, J., Prado, J.M., Isturiz, A., Gonzalez, C.: Flow regime analyses during the filling stage in powder metallurgy processes: Experimental study and numerical modelling. Granul. Matter **13**, 79–92 (2011)
12. Nosewicz, S., Rojek, J., Chmielewski, M., Pietrzak, K.: Discrete element modeling of intermetallic matrix composite manufacturing by powder metallurgy. Materials **12**(2), 281 (2019)
13. Zhou, S., Ren, Z., Zhang, Y., Ju, J.: Analysis of flow characteristics of granular material unloaded on nonlinear vibration inclined platform. Applied Mathematical Modelling **78**, 57–74 (2020)
14. Ogunmodimu, O., Govender, I., Mainza, A.N., Franzidis, J.P.: Development of a mechanistic model of granular flow on vibrating screens. Miner. Eng. **163**, 106771 (2021)
15. Yu, C., Wang, X., Gong, S., Pang, K., Zhao, G., Zhou, Q., Lin, D., Xu, N.: Stability analysis of the screening process of a vibrating flip-flow screen. Miner. Eng. **163**, 106794 (2021)
16. Regassa, B., Xu, N., Mei, G.: An equivalent discontinuous modeling method of jointed rock masses for DEM simulation of mining-induced rock movements. Int. J. Rock Mech. Min. Sci. **108**, 1–14 (2018)
17. Grieves, C.G., Crame, L.W., Venardos, D.G., Ying, W.C.: Powdered versus granular carbon for oil refinery wastewater treatment. J Water Pollut Control Feder **52**(3), 483–497 (1980)
18. Santoni, R.L., Tingle, J.S., Webster, S.L.: Engineering properties of sand-fiber mixtures for road construction. Journal of Geotechnical and Geoenvironmental Engineering **127**(3), 203–295 (2001)
19. Walton, O. Challenges in transporting, handling and processing regolith in the lunar environment, in *Moon, Prospective Energy and Material Resources* Viorel Badescu (Ed.) (Springer, 2012)
20. Horabik, J., Molenda, M.: Parameters and contact models for DEM simulations of agricultural granular materials: A review. Biosys. Eng. **147**, 206–225 (2016)
21. Sakaguchi, E., Suzuki, M., Favier, J.F., Kawakami, S.: Numerical simulation of the shaking separation of Paddy and Brown rice using the discrete element method. J Agric Eng Res **79**, 307–315 (2001). https://doi.org/10.1006/jaer.2001.0706
22. Li, J., Webb, C., Pandiella, S.S., Campbell, G.M.: A numerical simulation of separation of crop seeds by screening: effect of particle bed depth. Food Bioprod Process Trans Inst Chem Eng Part C **80**, 109–117 (2002). https://doi.org/10.1205/096030802529387 44
23. Goldhirsch, I.: Rapid granular flows. Annu. Rev. Fluid Mech. **35**, 267–293 (2003)
24. Forterre, Y., Pouliquen, O.: Flows of dense granular media. Annu. Rev. Fluid Mech. **40**, 1–24 (2008)
25. Lappa, M. On the nature of fluid-dynamics, Chapter 1 (pp. 1–64) In: Understanding the Nature of Science, Patrick Lindholm Editor, Nova Science Publishers Inc., Series: Science, Evolution and Creationism (2019). https://novapublishers.com/shop/understanding-the-nature-of-science/
26. Noirhomme, M., Cazaubiel, A., Darras, A., Falcon, E., Fischer, D., Garrabos, Y., Lecoutre-Chabot, C., Merminod, S., Opsomer, E., Palencia, F., Schockmel, J., Stannarius, R., Vandewalle, N.: Threshold of gas-like to clustering transition in driven granular media in low-gravity environment. Europhys. Lett. **123**(1), 14003 (2018)
27. Noirhomme, M., Cazaubiel, A., Falcon, E., Fischer, D., Garrabos, Y., Lecoutre-Chabot, C., Mawet, S., Opsomer, E., Palencia, F., Pillitteri, S., Vandewalle, N.: Particle dynamics at the onset of the granular gas-liquid transition. Phys. Rev. Lett. **126**, 128002 (2021)
28. Tsimring, L.S., Aranson, I.S.: Localised and cellular patterns in a vibrated granular layer. Phys. Rev. Lett. **79**(2), 213–216 (1997)
29. Irving, J.H., Kirkwood, J.G.: The statistical mechanical theory of transport processes. IV. The equations of hydrodynamics. J. Chem. Phys. **18**(6), 817–829 (1950)
30. Nicot, F., Hadda, N., Guessasma, M., Fortin, J., Millet, O.: On the definition of the stress tensor in granular media. Int. J. Solids Struct. **50**(14–15), 2508–2517 (2013)
31. Smith, A.L., Wensrich, C.M.: The effects of particle dynamics on the calculation of bulk stress in granular media. Int. J. Solids Struct. **51**, 4414–4418 (2014)
32. Thomas, B., Mason, M.O., Liu, Y.A., Squires, A.M.: Identifying states in shallow vibrated beds. Powder Technology **57**, 267–280 (1989)
33. Melo, F., Umbanhowar, P., Swinney, H.L.: Transition to parametric wave patterns in a vertically oscillated granular layer. Phys. Rev. Lett. **72**, 172 (1994)
34. Melo, F., Umbanhowar, P., Swinney, H.L.: Hexagons, kinks, and disorder in oscillated granular layers. Phys. Rev. Lett. **75**(21), 3838–3841 (1995)
35. Umbanhowar, P.B., Melo, F., Swinney, H.L.: Localised excitations in a vertically vibrated granular layer. Nature **382**, 793–796 (1996)
36. Bizon, C., Shattuck, M.D., Swift, J.B., McCormick, W.D., Swineey, H.L.: Pattern in 3D vertically oscillated granular layers: simulation and experiment. Phys. Rev. Lett. **80**, 57–60 (1998)
37. Guo, Y. & Curtis, J. S. Discrete element method simulations for complex granular flows. Annu. Rev. Fluid Mech (2014)
38. Kieckhefen, P., Pietsch, S., Dosta, M., Heinrich, S.: Possibilities and limits of computational fluid dynamics–discrete element method simulations in process engineering: A review of recent advancements and future trends. Annu. Rev. Chem. Biomol. Eng. **11**, 397–422 (2020)
39. El-Emam, M.A., Zhou, L., Shi, W., Han, C., Bai, L., Agarwal, A.: Theories and applications of CFD–DEM coupling approach for granular flow: A review. Archives of Computational Methods in Engineering **28**, 4979–5020 (2021)

40. Watson, P., Bonnieu, S.V., Lappa, M.: Fluidization and transport of vibrated granular matter: A review of landmark and recent contributions. Fluid Dynamics & Materials Processing **20**(1), 1–29 (2024)
41. Stratton, R.E., Wensrich, C.M.: Modelling of multiple intra-time step collisions in the hard-sphere discrete element method. Powder Technol. **199**(2), 120–130 (2010)
42. Richardson, D.C., Walsh, K.J., Murdoch, N., Michel, P.: Numerical simulations of granular dynamics: I. Hard-sphere discrete element method and tests. Icarus **212**(1), 427–437 (2011)
43. Schwartz, S.R., Richardson, D.C., Michel, P.: An implementation of the soft-sphere discrete element method in a high-performance parallel gravity tree-code. Granular Matter **14**, 363–380 (2012)
44. Murphy, E., Subramaniam, S.: Binary collision outcomes for inelastic soft-sphere models with cohesion. Powder Technol. **305**, 462–476 (2017)
45. Walton, O.R., Braun, R.L.: Viscosity, granular-temperature, and stress calculations for shearing assemblies of inelastic, frictional disks. J Rheol **30**, 949–980 (1986). https://doi.org/10.1122/1.549893
46. Walton, O.R.: Numerical simulation of inelastic, frictional particle-particle interactions. Particulate Two-Phase Flow **25**, 884–911 (1993)
47. Fonte, C. B., Oliveira, A. A. O. Jr, & De Almeida, L. C. DEM-CFD coupling: Mathematical modelling and case studies using Rocky-Dem ® and Ansys Fluent®. In: Eleventh International Conference on CFD in the Minerals and Process Industries 1–7 (CSIRO Organization, 2015)
48. Vivacqua, V., López, A., Hammond, R., et al.: DEM analysis of the effect of particle shape, cohesion and strain rate on powder rheometry. Powder Technol **342**, 653–663 (2019). https://doi.org/10.1016/j.powtec.2018.10.034
49. Ansys-Rocky DEM Technical Manual, 2023, version R2
50. Khiripet, N., Khantuwan, W., Jungck, J.R.: Ka-me: A Voronoi image analyzer. Bioinformatics **28**(13), 1802–1804 (2012). https://doi.org/10.1093/bioinformatics/bts253
51. Jungck, J.R., Pelsmajer, M.J., Chappel, C., Taylor, D.: Space: The re-visioning frontier of biological image analysis with graph theory, computational geometry, and spatial statistics. Mathematics **9**(21), 2726 (2021)
52. Clément, E., Vanel, L., Rajchenbach, J., Duran, J.: Pattern formation in a vibrated granular layer. Phys. Rev. E **53**(3), 2972–2975 (1996)
53. Clément, E., Labous, L.: Pattern formation in a vibrated granular layer: The pattern selection issue. Phys. Rev. E **62**, 8314 (2000)
54. Breu, A.P.J., Ensner, H.M., Kruelle, C.A., Rehberg, I.: Reversing the Brazil-nut effect: Competition between percolation and condensation. Phys. Rev. Lett. **90**(1), 014302 (2003)
55. Schroter, M., Ulrich, S., Kreft, J., Swift, J.B., Swinney, H.L.: Mechanisms in the size segregation of a binary granular mixture. Physical Review E — Statistical Nonlinear, and Soft Matter Physics **74**(1), 011307–011314 (2006)
56. Jain, A., Metzger, M.J., Glasser, B.J.: Effect of particle size distribution on segregation in vibrated systems. Powder Technol. **237**, 543–553 (2013)
57. Gray, J.M.N.T., Thornton, A.R.: A theory for particle size segregation in shallow granular free-surface flows. Proceedings of the Royal Society A: Mathematical, Physical and Engineering Sciences **461**(2057), 1447–1473 (2005)
58. Kolmogorov, A. N. The local structure of turbulence in incompressible viscous fluids at very large Reynolds numbers. Dokl. Akad. Nauk. SSSR **30**, 299–303 (1941). Reprinted in Proc. R. Soc. London A 434 9–13 (1991).
59. Kolmogorov, A.N.: On the degeneration of isotropic turbulence in an incompressible viscous fluids. Dokl. Akad. Nauk SSSR **31**, 538–541 (1941)
60. Kolmogorov, A.N.: Dissipation of energy in isotropic turbulence. Dokl. Akad. Nauk SSSR **32**, 19–21 (1941)
61. Kolmogorov, A.N.: Equations of turbulent motion in an incompressible fluid. Izv. Akad. Nauk. SSSR ser. Fiz. **6**, 56–58 (1942)
62. Taguchi, Y.-H.: k-5/3 Power spectrum in powder-turbulent flow in a vibrated bed: Numerical results. Europhys. Lett. **24**(3), 203–209 (1993)
63. Radjai, F., Roux, S.: Turbulent-like fluctuations in quasistatic flow of granular media. PhyS. Rev. Lett. **89**(6), 064302 (2002)
64. Busse, F.H.: The stability of finite amplitude cellular convection and its relation to an extremum principle. J. Fluid Mech. **30**, 625–649 (1967)
65. Roy, A., Steinberg, V.: ReEntrant hexagons in non-Boussinesq Rayleigh–Bénard convection: Effect of compressibility. Phys. Rev. Lett. **88**, 244503 (2002)
66. Madruga, S., Riecke, H., Pesch, W.: Re-entrant hexagons in non-Boussinesq convection. J. Fluid Mech. **548**, 341–360 (2006)
67. Kramers, H.A.: Het gedrag van macromoleculen in een stroomende vloeistof. Physica **11**, 1–19 (1944)
68. Giesekus, H.: Die Elastizität von Flüssigkeiten. Rheol. Acta **5**, 29–35 (1966)
69. Revuz, D. & Yor, M. Continuous Martingales and Brownian Motion. Grundlehren der Mathematischen Wissenschaften [Fundamental Principles of Mathematical Sciences] Volume 293, (Springer, 1994).
70. Lappa, M., Ferialdi, H.: Multiple solutions, oscillons and strange attractors in thermoviscoelastic marangoni convection. Physics of Fluids **30**(10), 104104 (2018)